mtDNA breaks compromise mitochondrial membrane ultrastructure and trigger an integrated stress response

Yi Fu[1,2], Evgeny Kanshin[3], Beatrix Ueberheide[3,4,5,6], and Agnel Sfeir[2]*

1- Skirball Institute of Biomolecular Medicine, Cell Biology Department, NYU School of Medicine, New York, NY, 10016
2- Molecular Biology Program, Sloan Kettering Institute, Memorial Sloan Kettering Cancer Center, New York, NY, 10065
3- Proteomics Laboratory, NYU School of Medicine, New York, NY, 10016
4- Biochemistry and Molecular Pharmacology, NYU School of Medicine, New York, NY, 10016
5- Department of Neurology, NYU School of Medicine, New York, NY, 10016
6- Perlmutter Cancer Center, NYU School of Medicine, New York, NY, 10016

*Correspondence:
Agnel Sfeir
430 E 67th Street – RRL 1141
New York, NY, 10065
Tel: 212-639-7095
SfeirA@mskcc.org

Mitochondrial DNA (mtDNA) breaks are deleterious lesions that lead to degradation of mitochondrial genomes and subsequent reduction in mtDNA copy number. The signaling pathways activated in response to mtDNA damage remain ill-defined. Using mitochondrial targeted restriction enzymes, we show that cells with mtDNA breaks exhibit reduced respiratory complexes, loss of membrane potential, and mitochondrial protein import defect. Furthermore, mtDNA damage activates the integrated stress response (ISR) through phosphorylation of eIF2α by the OMA1-DELE1-HRI pathway. Electron microscopy reveals concomitant defects in mitochondrial membranes and cristae ultrastructure. Notably, inhibition of the ISR exacerbates mitochondrial defects and delays the recovery of mtDNA copy number, thereby implicating this stress response in mitigating mitochondrial dysfunction following mtDNA damage. Last, we provide evidence suggesting that ATAD3A, a membrane-anchored protein that interacts with nucleoids, relays the signal from mtDNA breaks to the inner mitochondrial membrane. Altogether, our study fully delineates the sequence of events linking damaged mitochondrial genomes with the cytoplasm and uncovers an unanticipated role for the ISR in response to mitochondrial genome instability.

Introduction:

Mitochondria contain their own genomes, a multi-copy circular DNA encoding 37 genes that are essential for oxidative phosphorylation (OXPHOS)[1]. Mitochondrial DNA (mtDNA) is packaged with TFAM into nucleoids and is closely associated with the inner mitochondrial membrane (IMM)[1, 2]. mtDNA damage accumulates due to errors during replication and can also result from other endogenous and exogenous sources, including reactive oxygen species and radiation[3]. In contrast to the nucleus that is equipped with robust DNA damage signaling and repair pathways, mammalian mitochondria have limited DNA repair capabilities. Repairing mtDNA double-strand breaks (mtDSBs) – derived either from direct breaks or upon replication of un-repaired DNA nicks – is extremely rare and leads to mtDNA deletions[4] that underlie severe mitochondrial pathologies such Pearson's syndrome, Kearns-Sayre syndrome (KSS) and chronic progressive external ophthalmoplegia (CPEO)[5]. Instead, the majority of broken mtDNA is degraded by exonuclease activities of polymerase POLG and the mitochondrial genome maintenance exonuclease 1 (MGME1), leading to loss of mtDNA copy number[6, 7]. Replenishment of mtDNA molecules is contingent on replication of intact genomes. Given that factors required for mtDNA replication and maintenance are encoded by the nuclear genome, mitochondria-nuclear communication is critical to respond to various mtDNA perturbation. Currently, how mtDSBs are sensed by the cell remains poorly understood.

Mitochondria-nuclear crosstalk, exemplified by retrograde signaling, involves direct inter-organellar contacts, small messenger metabolites, as well as transcriptional and translational programs[8]. Retrograde signaling was initially discovered in yeast, where a group of transcription factors termed RTGs relocate from the mitochondria to the nucleus in response to mitochondrial respiration deficiency and turn on metabolic genes[9]. RTG genes are not conserved in higher eukaryotes. Rather, retrograde signaling in metazoa invokes the mitochondrial unfolded protein response (UPR^{mt}), a transcription program that promotes repair and recovery from various forms of mitochondrial dysfunction including perturbations in oxidative phosphorylation (OXPHOS), mitochondrial protein synthesis, protein import, and mtDNA mutations[10]. The mechanism of UPR^{mt} is most well characterized in *C. elegans*, where the key transcription factor ATFS-1 fails to be imported into dysfunctional mitochondria, thereby relocating to the nucleus to trigger downstream UPR^{mt} gene activation. In mammalian cells, a central element of the UPR^{mt} is the integrated stress response (ISR), an adaptive pathway that responds to a diverse set of stress stimuli to re-establish cellular homeostasis[11]. The core event in ISR is the phosphorylation of eukaryotic translation initiation factor 2 alpha (eIF2α) by four kinases, HRI, GCN2, PERK, and

PKR that sense different types of stresses. Activation of eIF2α reduces global translation except for a subset of stress-related mRNAs, including CHOP, ATF4, and ATF5[12]. These transcription factors localize to the nucleus and activate genes involved in proteostasis and metabolic remodeling. Recent work has identified another form of retrograde signaling, which is based on mitochondrial nucleic acids being released into the cytoplasm to engage with cytoplasmic pattern recognition receptors and activate the innate immune response[13-18].

Here we systematically delineate the cellular response to mtDNA damage. We show that a subset of cells bearing damaged mitochondrial genomes display abnormal cristae morphology and activate the ISR in an OMA1-DELE1-HRI dependent manner[19, 20]. We also identify ATAD3A, a AAA+-ATPase located at the inner mitochondrial membrane, as a key factor that transmits the message from defective genomes to mitochondrial membranes. Collectively, our findings provide a framework by which an organelle with limited DNA repair capabilities engages with cytoplasmic signaling pathways to mitigate the dysfunction in response to mtDNA instability.

Results:

BioID-based proteomic profiling reveals changes in nucleoid composition in response to mtDSBs

To generate mtDNA breaks in a controlled manner, we transduced retinal pigmental epithelial cells (ARPE-19) with lentivirus expressing mitochondrial targeted ApaLI under a doxycycline (Dox) inducible promote. When localized to the mitochondria, ApaLI cleaves the MT-RNR1 locus that encodes the 12S rRNA[21] (Fig. 1a). Induction of ApaLI resulted in expected mtDNA depletion and subsequent loss of TFAM protein (Fig. 1b,c, Extended Data Fig. 1a, b). As expected, turning off ApaLI expression was followed by a gradual repopulation of mtDNA copy number over ~50 days (Fig. 1b,c)[22]. As a control, we generated a catalytically inactive ApaLI (termed ApaLI*) with three base substitutions at the predicted active site (D211DA, E225A, K227A)[23], and confirmed that mtDNA depletion results from an mtDNA break when induced by a catalytically active ApaLI (Extended Data Fig. 1c,d).

We reasoned that factors that sense mtDNA damage are likely to be recruited to the nucleoids shortly after break formation, prompting us to develop a proteomic-based approach to survey the interactome of mitochondrial nucleoids. We combined proximity-dependent biotin labeling with quantitative proteomics that utilizes Stable Isotope Labeling by Amino acids in Cell culture

(SILAC)[24] (Fig. 1d,e). We transduced ARPE-19 cells expressing ApaLI and ApaLI* with TFAM-BioID2[25]. The fusion protein was properly localized to the mitochondria and its expression did not significantly alter mtDNA copy number (Extended Data Fig. 1e,f). To barcode different samples, we labeled the proteomes of cells expressing different transgenes by culturing them for 10 population doublings in media containing heavy (H), medium (M), and light (L) isotopes of lysine and arginine (Fig. 1e). We then treated labeled cells for 12 hours with doxycycline to induce the expression of ApaLI and ApaLI* (named as sample *ApaLI* and *ApaLI**, respectively) and biotin to biotinylate lysine residues on proteins adjacent to the TFAM-BioID2 bait (Fig. 1e). It is worth noting that within 12 hours of ApaLI induction, a fraction of mtDNA molecules were cleaved and linear fragments were still detectable and therefore not fully degraded (Extended Data Fig. 1b). Samples corresponding to *ApaLI* and *ApaLI** were collected, lysed, and pooled together with a control sample not treated with biotin (named *No Biotin*) (Fig. 1e, Extended Data Fig. 1g). Ultimately, biotinylated proteins were captured with streptavidin beads and subjected to mass spectrometry analysis.

To highlight the full spectrum of nucleoid-associated proteins captured in the vicinity of TFAM-BioID2, we calculated the SILAC ratio[26] of peptides retrieved from cells treated with biotin (*ApaLI* and *ApaLI**) compared to "*No biotin"* control. Our analysis identified 68 and 94 proteins (1.5 fold change, ≥ 2 replicates) that were proximal to nucleoids in cells expressing ApaLI and ApaLI*, respectively (Extended Data Fig. 1h, 2a). Over 70% of these potential nucleoid-associated factors were previously detected in the mitochondria according to MitoCarta 3.0[27], including several nucleoid associated proteins (curated in [28]) (Extended Data Fig. 2a,b). To capture changes in nucleoid composition following DNA breaks, we calculated the SILAC ratio of proteins retrieved in *ApaLI* relative to *ApaLI** and normalized to TFAM-BioID2 (Extended Data Fig. 1h, 2c). Based on our analysis, we identified 24 proteins that were depleted in response mtDNA breaks (1.2 fold change, ≥ 2 replicates), including expected nucleoid factors Twinkle, mtSSB and SHMT2 (Fig. 1e,f). Numerous mitochondria ribosomal proteins were also depleted, suggesting that ribosome assembly in adjacent mitochondrial RNA granules could be altered in response to mtDNA damage (Extended Data Fig. 2d)[29, 30]. On the other hand, 28 proteins were enriched at nucleoids carrying mtDNA breaks, including 16 matrix-residing and IMM associated factors, as well as 12 factors that had not previously been detected in the mitochondria (Fig. 1h,i, Extended Data Fig. 2e). We suspected that factors involved in mtDNA damage signaling to be among the enriched proteins in the proteomic experiment.

Defective mitochondrial protein import in response to mtDNA breaks

We were intrigued by hits that were detected in the vicinity of TFAM-BioID2 but not been previously reported in the mitochondria. To confirm their recruitment to the mitochondria in response to mtDNA breaks, we employed a split-GFP system[31]. We targeted a truncated GFP protein composed of 10 β–strands (GFP1-10) to the mitochondrial matrix by appending it with a mitochondria-localization sequence (MLS). In parallel, we used CRISPR/Cas9 to knock-in a peptide coding for the eleventh β-strand (GFP11) at the 3' end of RRBP1, a rough endoplasmic reticulum protein[32] and two nuclear residing factors, MTA2 and SMCHD1 (Fig. 2a, Extended Data Fig. 3a). We monitored GFP reconstitution in RRBP1^{GFP11}, MTA2^{GFP11}, and SMCHD1^{GFP11} with flow cytometry and observed an increase in the percentage of GFP positive (GFP+) cells upon ApaLI-induced mtDNA cleavage (Fig. 2b, Extended Data Fig. 3b).

Surprisingly, upon examining the localization of GFP using fluorescent microscopy, we observed that the signal was not in the mitochondria, but rather at the rough ER in RRBP1^{GFP11}, and in the nucleus in MTA^{GFP11} and SMCHD1^{GFP11} cells (Fig. 2c, Extended Data Fig. 3c,d). Based on these results, we concluded that in a subset of cells subjected to mtDNA breaks, mito-GFP1-10 is mistargeted to the cytoplasm and the nucleus. To corroborate these findings, we targeted GFP11 to 5'-end of a list of ER (KTN1, VAPB, CANX, SEC61B) and Golgi (ARL1) residing proteins that were neither associated with the mitochondria based on the literature, nor detected in the proteomic screen (Extended Data Fig. 3a). Consistent with sequestration of mito-GFP1-10 away from the mitochondria, the reconstituted GFP signal was present at ER and Golgi in a small but significant fraction of cells exposed to mtDNA breaks (Fig. 2d,e and Extended Data Fig. 3b,d).

Given that cleaved mtDNA molecules are ultimately degraded (Fig. 1b, Extended Data Fig. 1b)[6, 7, 22], it was imperative to rule out that the mis-localization of mito-GFP1-10 in ApaLI expressing cells was due to the loss of mtDNA. To that end, we treated MTA^{GFP11} cells with the chain terminator 2′,3′-dideoxycytidine (ddC) for 7 days that led to the expected depletion of mtDNA (Extended Data Fig. 4a). However, despite the loss of mtDNA, there was no significant accumulation of GFP+ cells (Extended Data Fig. 4b), indicating that mis-localization of mito-GFP1-10 is caused by broken mtDNA molecules. To corroborate the defective import of mito-GFP1-10 in response to mtDSBs, we performed subcellular fractionation followed by Western blot and detected significant accumulation of GFP1-10 precursors in the cytosolic fraction of GFP+ cells sorted from a population of ApaLI induced cells (Fig. 2f,g, Extended Data Fig. 4c). These results were further supported by the evidence that overexpression of frataxin – a protein with well-defined isoforms indicative of mitochondrial import and processing[33, 34] – resulted in

accumulation of precursors in settings of mtDSB formation (Extended Data Fig. 3d,e). In addition, we detected a reduction in the levels of several matrix residing proteins, including POLG, Twinkle, MGME1 and LRPPRC (Fig. 2g, Extended Data Fig. 4c), which is potentially indicative of a broader mitochondrial protein import as the consequence of mtDSBs. Taken together, our data provide evidence that mtDNA breaks elicit mitochondrial dysfunction that in turn manifest in protein import defect.

Activation of the integrated stress response in a subset of cells subjected to mtDSBs

To gain further insight into the mitochondrial defect in response to mtDSBs, we induced mtDNA breaks in MTA2^{GFP11} cells and sorted for GFP+ cells (Fig. 2f). In addition to transient impairment of cellular growth (Fig. 2h), GFP+ cells displayed decreased membrane potential, severe loss of multiple OXPHOS components, and increased autophagy, noted by LC3-I to LC3-II conversion (Extended Data Fig. 4f-j). To investigate transcriptional changes in cells with mis-localized mito-GFP1-10, we performed RNA-seq analysis and identified 558 genes (116 up-regulated, 442 down-regulated) that were deregulated in GFP+ cells relative to control cells (Fig. 3a). Gene Set Enrichment Analysis (GSEA) revealed several biological processes that were significantly altered, including upregulation of the inflammatory response pathway, and down-regulation of mitotic genes (Fig. 3b, Extended Data Fig. 5a). Notably, the unfolded protein response (UPR) pathway appeared to be specifically induced in GFP+ cells (Fig. 3b, Extended Data Fig. 5a).

Consistent with the integrated stress response being central to the mitochondrial UPR in mammalian cells, we demonstrated that many ISR target genes[19] were up-regulated in GFP+ cells (Fig 3c,d, Extended Data Fig. 5b). Furthermore, we detected increased eIF2α phosphorylation and accumulation of ATF4 and CHOP in GFP+ cells (Fig. 3e). To rule out that ISR activation due to mtDNA depletion, we showed that treatment of cells with ddC did not increase CHOP expression (Extended Data Fig. 5c). Lastly, we observed that withdrawal of Dox led to the silencing of CHOP. The latter observation is consistent with transient and reversible activation of ISR following mtDSB formation (Extended Data Fig. 5d).

OMA1 – DELE1 – HRI activates an acute ISR to mitigate mitochondrial dysfunction caused by mtDNA damage

Phosphorylation of eIF2α is mediated by four kinases: HRI, PKR, PERK, GCN2, each acting in response to different stress stimuli[12, 35]. Specifically, in response to OXPHOS inhibition and

membrane depolarization the inner membrane protease, OMA1 cleaves DELE1 and prompts its re-localization from the intermembrane space to the cytosol, where it engages with and activates HRI[19, 20, 36]. To determine the kinase that phosphorylates eIF2α in response to mtDSBs, we used CRISPR/Cas9 and individually depleted the four kinases in MTA2^{GFP11} cells (Extended Data Fig. 6a). We next induced ApaLI expression and monitored CHOP and ATF4 levels in resultant GFP+ cells. As a control, we showed that treating cells with a small-molecule ISR inhibitor (ISRIB) that suppresses eIF2a phosphorylation[12, 37-39], reduced the level of CHOP and ATF4 in GFP+ cells (Fig. 4a). Depletion of HRI, but not PKR, PERK or GCN2 led to an attenuation of the ISR (Fig. 4a). We observed a similar effect in the absence of DELE1 and to a lesser extent, when we depleted OMA1 (Fig. 4a, Extended Data Fig. 6b). These results implicate the OMA1-DELE1-HRI pathway in the activation of ISR in response to mtDSBs.

To better understand the significance of an ISR in cells withstanding mtDNA damage, we treated MTA2^{GFP11} cells with ISRIB and sgRNAs targeting OMA1, DELE1, and HRI, independently (Extended Data Fig. 6c). We then induced mtDNA breaks and noticed a significant increase in the percentage of GFP+ cells when ISR was blocked. In effect, this stress response appears to counteract the mitochondrial protein import defect due to mtDSB accumulation (Fig. 4b, Extended Data Fig. 6d). In addition, we showed that ISRIB treatment delayed mtDNA copy number recovery following withdrawal of ApaLI (Fig. 4c, Extended Data Fig. 6e,f). In conclusion, our data underscore a pro-survival and adaptive function for the ISR to counteract mitochondrial defects elicited by mtDNA damage, allow mtDNA copy number recovery, and reestablish cellular homeostasis.

mtDNA damage leads to defective mitochondrial membrane ultrastructure

So far, our study uncovered a critical function for the ISR downstream of mtDNA damage and implicated the OMA1-DELE1-HRI axis in the phosphorylation of eIF2α. Given the close association of nucleoids with the IMM[1, 2], we speculated that mtDSBs might impair mitochondrial membrane structure, which would then lead to loss of membrane potential and a plethoral of mitochondrial defects. Using transmission electron microscopy (TEM), we observed that mitochondria were markedly deformed in cells expressing ApaLI. Particularly, we noticed that GFP+ subpopulation exhibited severe abnormalities with notable accumulation of multi-membrane lysosomes[40] that is consistent with the increased LC3 conversion (Fig. 5a,b, Extended Data Fig. 4j, 7a). 3D reconstruction of the TEM images showed that mitochondria in cells expressing ApaLI lacked the typical lamellar structures and were devoid of cristae junctions.

Instead, cells incurring mtDSBs were enriched in vesicular and onion shape cristae, reminiscent of structures observed upon depletion of the MICOS complex (Fig. 5c, Extended Data Video. 1-5)[28]. Indeed, the severe cristae abnormalities evident under mtDNA cleavage was coupled to significant loss of MIC60 and MIC10, two core components of the MICOS complex (Fig. 5d).

Lastly, to identify factor(s) that could link defective mitochondrial genomes with mitochondrial membranes, we leveraged our proteomic analysis and focused on mitochondrial proteins that were enriched in the vicinity of nucleoids carrying mtDNA breaks (Extended Data Fig. 2e). We depleted candidate hits in MTA2^{GFP11} (and RRBP1^{GFP11}) cells and noticed that knock-down of ATAD3A with siRNA resulted in a significant increase in GFP+ cells in response to break formation (Extended Data Fig. 7b). ATAD3A is a conserved AAA+ ATPase that spans the IMM and simultaneously associates with the nucleoids in the matrix[41]. The anchor protein is well positioned to relay the signal from defective genomes to the mitochondrial membrane. We validated the results through CRISPR/Cas9 editing and observed severe mitochondrial protein mis-localization and ISR activation upon ATAD3A loss and regardless of mtDNA damage (Fig. 5e, Extended Data Fig. 7c,d). These results are consistent with ATAD3A functioning downstream of mtDNA damage to alter mitochondrial membrane structure and activated an ISR.

Discussion

It was noted ~50 years ago that the half-life of mtDNA is shorter than nuclear DNA[42] and rapid turn-over might prevent the accumulation of mutations in mitochondrial genomes[43]. DNA lesions including oxidized bases as well as unrepaired nicks can be converted to DSBs that lead to mtDNA degradation[44]. Increased replication of intact genomes is necessary to counterbalance mtDNA loss and is contingent on proper mitochondrial-nuclear communication. The cellular response to mtDSB has been largely ignored. Using a mitochondrial targeted restriction enzyme, we observed severe mitochondrial defects in a subpopulation of cells carrying mtDNA breaks, including loss of membrane potential, impaired mitochondrial protein import, defective cristae organization and slower cell growth. Concomitantly, we detected acute activation of the ISR through the phosphorylation of eIF2α by the OMA1-DELE1-HRI pathway. We propose a model whereby ISR activation is necessary to counteract mitochondrial import defect and supports the recovery of mtDNA copy number to ultimately re-establish mitochondrial function and ensure cellular homeostasis (Fig. 5f).

Interestingly, only a subset of cells (~15%) that receive mtDSBs display robust mitochondrial defect and ISR induction. It is possible that a certain threshold of cleaved genomes is necessary to trigger the response to mtDNA breaks. We disfavor this scenario since the loss of copy number, which serves as proxy for mtDNA breaks, was comparable in GFP+ and GFP- cells (Extended Data Fig. 6g). Instead, since the transient activation of the ISR suppresses mitochondrial defect, at a given time point only a subset of cells is expected display import defect and are captured as a GFP+. In support of this scenario, we show that inhibition of ISR augments protein import defect evident by increased mis-localization of mito-GFP1-10 and delayed mtDNA recovery after break formation (Fig. 4b-c).

Based on our data, we propose that deformation of mitochondrial membranes and loss of cristae junctions are central to triggering a cellular response to mtDSB and potentially underlie the activation of ISR. Altering mitochondrial membrane integrity and mitochondrial depolarization could hinder the import of DELE1, resulting in its cytoplasmic accumulation where it activates HRI[45]. This is consistent with previous literature indicating that mitochondrial import defect activates the ISR[36]. The defect could be augmented by the loss of MICOS complex (Fig. 5d), where disruption of the IMM, including the contact sites between IMM and OMM, could further activate OMA1 to cleave and release DELE1 to the cytoplasm[45, 46].

It has been established that nucleoids reside in between cristae and in proximity to the inner mitochondrial membrane[2, 47]. Cristae abnormalities associated with mtDSBs recapitulates observations in cells from patients harboring mtDNA mutations[48], suggesting that the inner mitochondrial membrane could act as a sensor of damaged genomes. Specifically, we propose that ATAD3A is the linchpin that connects mtDNA and the IMM. This is consistent with the scaffolding function of ATAD3A, interacting with the membrane organization machinery (OPA1, YME1L, prohibitin, and MICOS complexes)[49] while also associating with nucleoids[50, 51]. Paradoxically, our mass spectrometry data showed enhanced association of ATAD3A with nucleoids upon mtDNA breaks (Fig. 1h). It is possible that the affinity of ATAD3A to mtDNA is dependent on DNA supercoiling, and thus, its binding to relaxed DNA triggers a conformational shift that would impair the scaffolding role of the AAA+ ATPase. One can also envision that a conformational change in ATAD3A bound to linear DNA could interfere its ability to oligomerize, a step that was previously implicated in mitochondrial fragmentation and mtDNA stability[52]. To that end, biophysical and structural studies are necessary to elucidate the underpinnings of this process.

Ultimately, while our study uncovered ISR activation in response to exogenously induced mtDNA breaks, our findings are likely to have implications to a wider range of pathological mtDNA perturbations. Disease models associated with defective exonuclease activity of POLG and MGME1 accumulate linear mtDNA and exhibit increased level of fibroblast growth factor 21 (FGF21), downstream of ATF4[6, 7, 53-55]. It has also been reported that mutations in TWINKLE helicase, which lead to mtDNA replication defect, activate the ISR[56, 57]. In summary, our study adds mtDNA breaks to the repertoire of defects eliciting an ISR in mammalian cells. A better understanding of ISR in mitochondrial DNA diseases could provide potential therapeutic insights.

Acknowledgements We thank Carlos Moraes for providing the mito-ApaLI plasmid. We thank the Proteomics Laboratory at NYU Langone Health, supported in part by NYU Langone Health and the Laura and Isaac Perlmutter Cancer Center support grant P30CA016087 from the National Cancer Institute. We acknowledge support of the Integrated Genomics Operation Core at MSKCC, funded by the NCI Cancer Center Support Grant (CCSG, P30 CA08748), Cycle for Survival, and the Marie-Josée and Henry R. Kravis Center for Molecular Oncology. We also acknowledge NYU Langone Health DART Microscopy Lab, partially funded by NYU Cancer Center Support Grant NIH/NCI P30CA016087, for assistance with TEM work. We thank members of the Sfeir lab for feedback on the manuscript. This work was supported by grants from the Pew Charitable Trust, The G. Harold & Leila Y. Mathers Charitable Foundation, and the Edward Mallinckrodt Jr. Foundation Award (A.S.).

Authors Contribution A.S. and Y.F. conceived the experimental design and wrote the manuscript. Y.F performed all experiments. E.K and B.U. performed mass spectrometry and analysis. All authors discussed the results and commented on the manuscript.

Authors information Agnel Sfeir is a co-founder, consultant, and shareholder of Repare Therapeutics. Correspondence and requests for materials should be addressed to A.S. sfeira@mskcc.org.

Figure legends:

Figure 1 | BioID-based proteomic analysis reveals changes in nucleoid composition in response to mtDSBs. a, Schematic of mtDSB formation by a mitochondria-localized restriction enzyme ApaLI that recognizes sequences in the 12S rRNA and is controlled by a doxycycline (Dox) inducible promoter. **b**, Temporal copy number dynamics of mtDNA in response to ApaLI-

induced DSBs in ARPE-19 cells, measured by qPCR of ND2 (mtDNA) relative to ACTIN locus. Cells expressing inducible ApaLI were treated with Dox on Day 0 and Dox was withdrawn on Day 3. Values at different time points were normalized to Day 0. Normalized copy numbers are means ± s.d. from n = 3 technical replicates. **c**, Western blot analysis of ApaLI (HA-tagged) and TFAM during ApaLI induction and recovery as per Fig. 1b. **d**, TFAM-BioID2 biotinylation to capture and identify mtDNA-associated proteins. **e**, Experimental design of a 3-state SILAC labeling used to identify mtDNA-associated proteins in response to mtDSBs. H/M/L, heavy/medium/light isotopes of lysine and arginine. PD, population doubling. **f**, SILAC ratio plot showing the TFAM-BioID2-normalized log2(*ApaLI*/*ApaLI**) against log2(*ApaLI**/*No Biotin*). 24 proteins depleted in *ApaLI* are highlighted in pink. Among them, 21 MitoCarta 3.0 proteins are marked in dark pink on the right. See Extended Data Fig. 2d for details. **g**, Categories of 24 proteins depleted in *ApaLI*. **h**, SILAC ratio plot showing the normalized log2(*ApaLI*/*ApaLI**) against log2(*ApaLI*/*No Biotin*). 28 proteins enriched in *ApaLI* are highlighted in green. Among them, 11 non MitoCarta 3.0 proteins are marked in dark green on the right. **i**, Categories of subcellular localization of 28 mtDSB-enriched proteins. Matrix, mitochondrial matrix; IMM, inner mitochondrial membrane; ER, endoplasmic reticulum; Cyto, cytoplasm; Nuc, nucleus.

Figure 2 | Defective mitochondrial protein import in response to mtDNA breaks. a, Schematic of the split-GFP used to assess mitochondrial localization of candidate proteins following mtDSBs. **b**, Flow cytometry analysis of GFP positive percentage in cells expressing mito-GFP1-10 and GFP11-tagged RRBP1 or MTA2 (referred as RRBP1^{GFP11} and MTA2^{GFP11}) under mtDSBs. RRBP1^{GFP11} and MTA2^{GFP11} cells expressing ApaLI or ApaLI* were treated with Dox for 2 days. **c**, Representative images of cellular localization of reconstituted split GFP in cells from Fig. 2b. Primary localization of the non-mitochondrial protein being tagged is labeled in parenthesis. RER, rough endoplasmic reticulum. Scale bar, 20 μm. **d**, Flow cytometry analysis of GFP positive percentage in cells that are expressing mito-GFP1-10 and GFP11-tagged CANX (CANX^{GFP11}), SEC61B (^{GFP11}SEC61B, overexpressed cDNA, N-terminally tagged) and ARL1 (ARL1^{GFP11}) under mtDSBs. CANX^{GFP11}, ^{GFP11}SEC61B, and ARL1^{GFP11} cells expressing ApaLI were treated with Dox for 2 days. Data in Fig. 2b,d are means ± s.d. of n = 3 to 5 biological replicates; one-way ANOVA. *$P \leq 0.05$, **$P \leq 0.01$, ***$P \leq 0.001$, ****$P \leq 0.0001$. **e**, Representative images of cellular localization of reconstituted split GFP in cells from d. Primary localization of the non-mitochondrial protein being tagged is labeled in parenthesis. Scale bar, 20 μm. **f**, Representative gating for fluorescence-activated cell sorting (FACS) of GFP negative (GFP-) and positive (GFP+) populations from MTA2^{GFP11} cells expressing ApaLI and ApaLI* and treated with

Dox for 2 days. **g**, Subcellular fractionation followed by Western blot analysis of the indicated proteins from MTA2^{GFP11} cells with indicated treatments, including cell sorting based on GFP. p, precursor isoform; m, mature isoform. See Extended Data Fig. 4c for more detail. **h**, Incucyte cell growth analysis of sorted GFP- and GFP+ populations of mtDSB-induced MTA2^{GFP11} cells. MTA2^{GFP11} cells expressing ApaLI were treated with Dox for 48 hours and subjected to sorting. Growth analysis was performed after Dox removal. Data are means ± SEM of n = 2 technical replicates.

Figure 3 | Acute activation of the integrated stress response in a subset of cells under mtDSBs. **a**, Heatmap depicting expression of 558 differentially expressed genes in GFP+ vs. GFP- RRBP1^{GFP11} cells with ApaLI induction (116 up-regulated, 442 down-regulated. 2 fold change cut-off, adjusted p-value < 0.01, n = 2 biological replicates). **b**, Gene Set Enrichment Analysis of differentially expressed genes depicted in Fig. 3a using MSigDB hallmark gene sets. Red bars indicating up-regulated pathways and blue bars representing down-regulated genes in GFP+ cells compared to GFP- cells. **c**, Volcano plot highlighting 116 up-regulated genes in GFP+ relative to GFP- subpopulations in red. ISR target genes are labeled with gene symbols. **d**, Heatmap showing the expression of ISR target genes (according to Fessler, et al. Nature. 2020.[19]). **e**, Western blot analysis of ATF4, CHOP, and phosphorylated eIF2α in GFP+ population of ApaLI induced RRBP1^{GFP11} and MTA2^{GFP11} cells, compared to GFP- and unsorted cells.

Figure 4 | OMA1 – DELE1 – HRI triggers an acute ISR to re-establish mitochondrial function. **a**, Western blot analysis of CHOP and ATF4 in the GFP+ populations of MTA2^{GFP11} cells that are under mtDSBs and subjected to indicated ISR inhibition treatments: ISRIB and CRISPR knock-out of DELE1, OMA1, HRI, GCN2, PERK and PKR. **b**, Percentage of GFP positive cells determined by flow cytometry analysis in MTA2^{GFP11} cells that are under mtDSBs and subjected to indicated ISR inhibition treatments. Data are means ± s.d. of n = 3 biological replicates; one-way ANOVA. P-value for ISRIB was calculated by comparing to Untreated. P-values for CRISPR treatment were calculated by comparing to NT (non-targeted gRNA). ns, $P \geq 0.05$. *$P \leq 0.05$, **$P \leq 0.01$, ***$P \leq 0.001$, ****$P \leq 0.0001$. **c**, Copy number dynamics of mtDNA in sorted GFP+ populations of MTA2^{GFP11} cells that are under mtDSBs with and without ISRIB treatment. MTA2^{GFP11} cells expressing ApaLI were treated with Dox at Day -3 and Dox was withdrawn at Day 0. Values at different time points were normalized to Day -3. Normalized copy numbers means ± s.d. from n = 3 technical replicates. See Extended Data Fig. 6d for additional biological replicates.

Figure 5 | Defective cristae in cells subjected to mtDNA damage. a, Representative TEM images of unsorted and GFP+ populations of MTA2^{GFP11} cells expressing ApaLI (and ApaLI*) and treated with Dox for 3 days. **b**, Violin plot presenting numbers of normal and abnormal mitochondria per field. Numbers of fields analyzed in total for ApaLI*+Dox, ApaLI+Dox, ApaLI+Dox GFP+ samples are 35, 48, 34, respectively. Two-way ANOVA. **c**, Representative TEM images of MTA2^{GFP11} cells expressing ApaLI* and ApaLI and treated with Dox for 3 days. Shown are 3D reconstructed mitochondria. **d**, Western blot analysis of MIC60, MIC10 and ATAD3A/B in MTA2^{GFP11} cells with indicated treatments. **e**, Percentage of GFP positive cells determined by flow cytometry analysis in MTA2^{GFP11} cells expressing ApaLI or ApaLI* and treated with sgRNA targeting ATAD3A and ATAD3B. Data are means ± s.d. of n = 2 biological replicates; two-way ANOVA. *$P \leq 0.05$, ****$P \leq 0.0001$. **f**, Working model – mtDNA breaks affect normal cristae morphology through ATAD3A and the MICOS complex, hinder protein import, and trigger mitochondrial dysfunction. ISR is activated to counteract mitochondrial defect, increase mtDNA copy number, and reestablish homeostasis.

Figure 1. Fu et al.

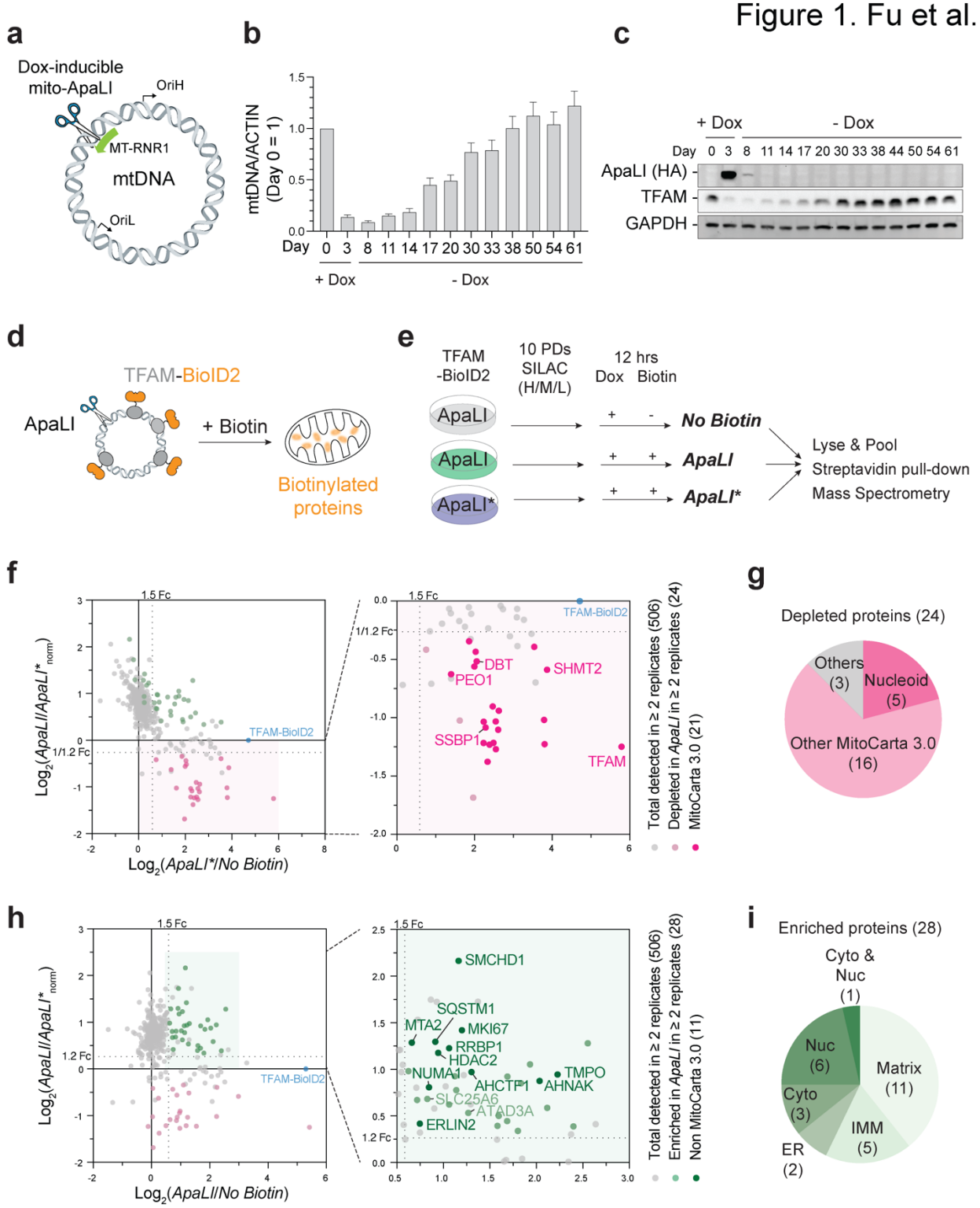

Figure 2. Fu et al.

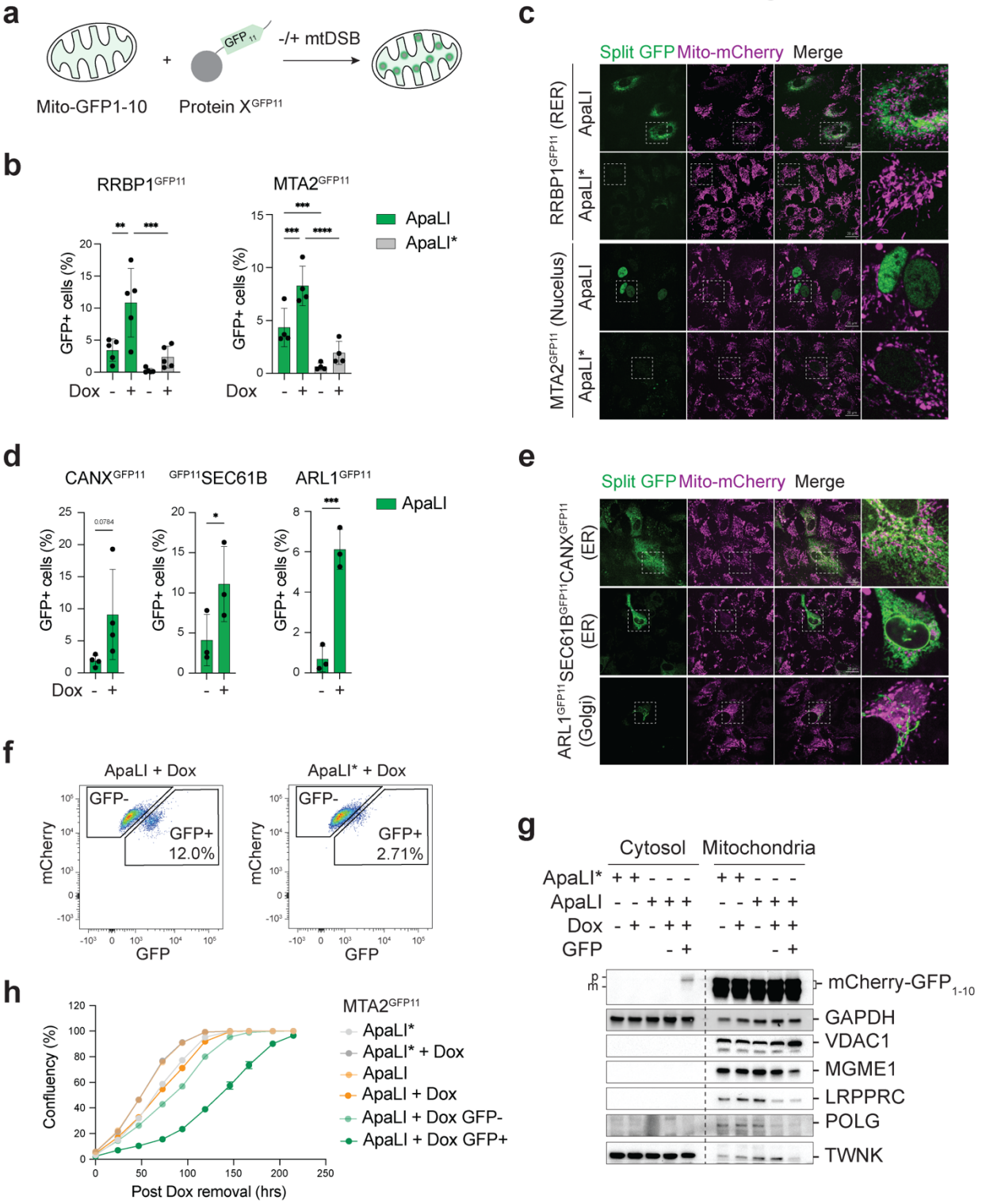

Figure 3. Fu et al.

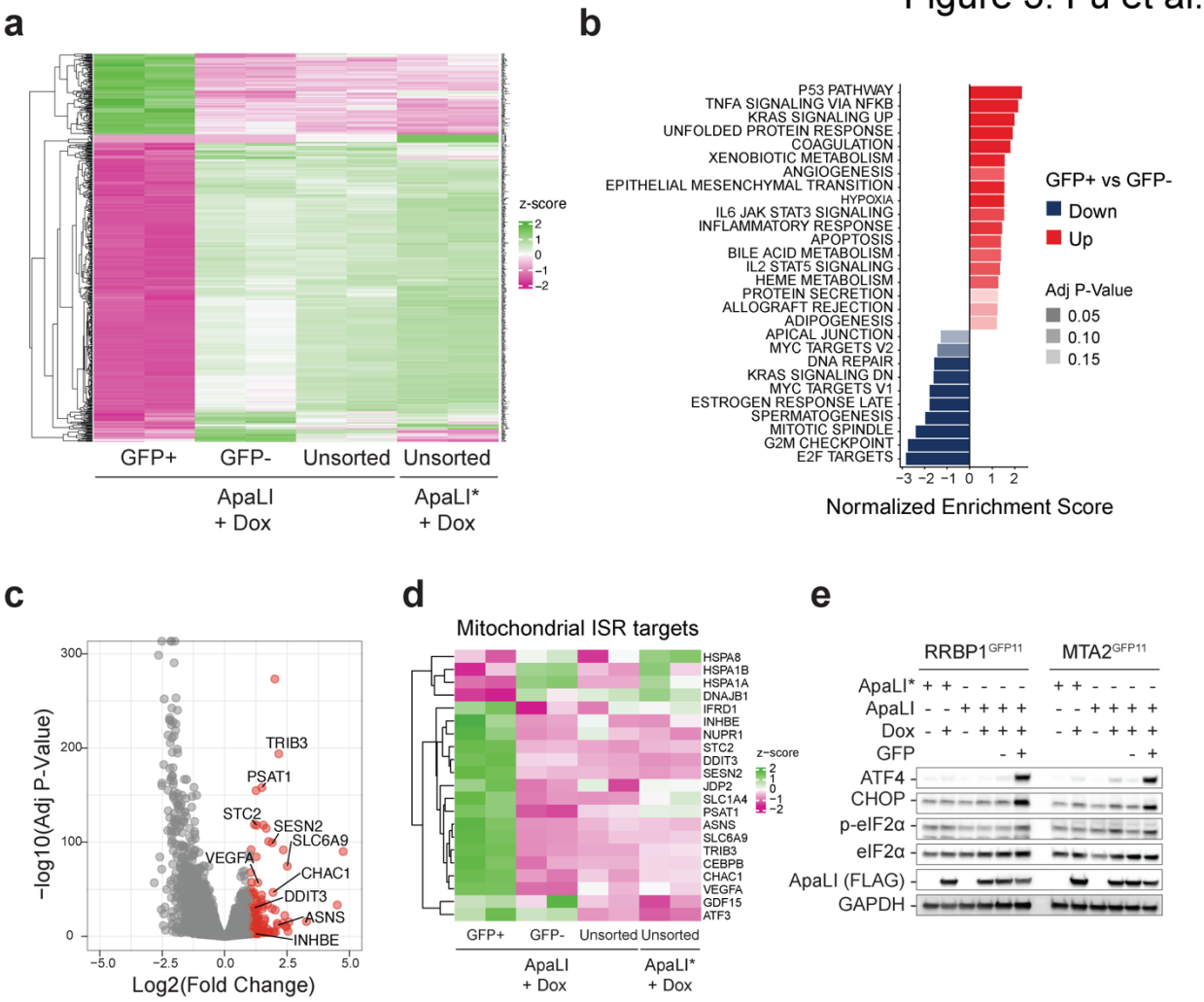

Figure 4. Fu et al.

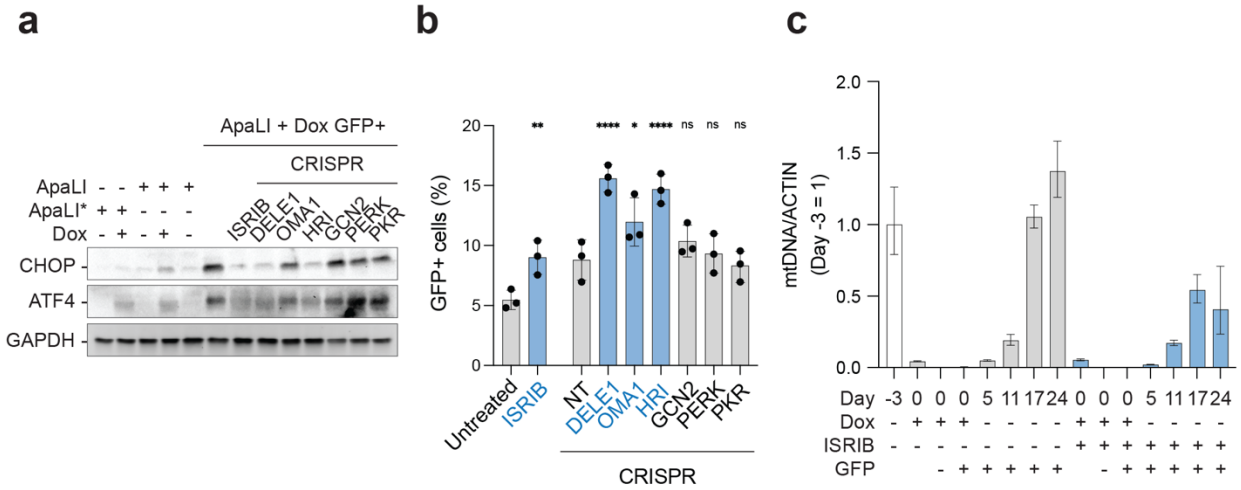

Figure 5. Fu et al.

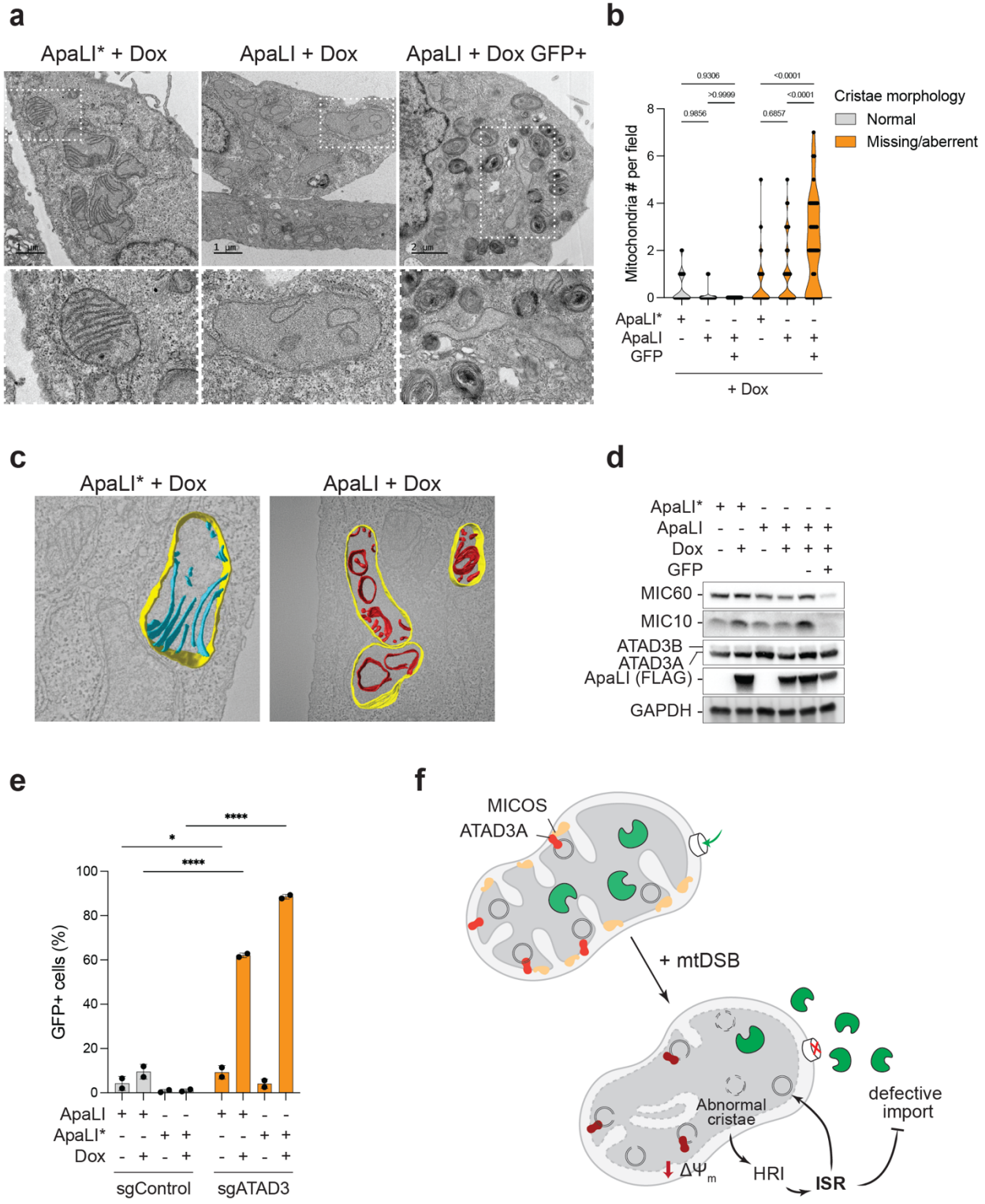

Reference:

1. Gustafsson, C.M., Falkenberg, M. & Larsson, N.G. Maintenance and Expression of Mammalian Mitochondrial DNA. *Annu Rev Biochem* **85**, 133-160 (2016).
2. Gerhold, J.M. *et al.* Corrigendum: Human Mitochondrial DNA-Protein Complexes Attach to a Cholesterol-Rich Membrane Structure. *Sci Rep* **5**, 17119 (2015).
3. Alexeyev, M., Shokolenko, I., Wilson, G. & LeDoux, S. The maintenance of mitochondrial DNA integrity--critical analysis and update. *Cold Spring Harb Perspect Biol* **5**, a012641 (2013).
4. Phillips, A.F. *et al.* Single-Molecule Analysis of mtDNA Replication Uncovers the Basis of the Common Deletion. *Mol Cell* **65**, 527-538 e526 (2017).
5. Tuppen, H.A., Blakely, E.L., Turnbull, D.M. & Taylor, R.W. Mitochondrial DNA mutations and human disease. *Biochim Biophys Acta* **1797**, 113-128 (2010).
6. Peeva, V. *et al.* Linear mitochondrial DNA is rapidly degraded by components of the replication machinery. *Nat Commun* **9**, 1727 (2018).
7. Nissanka, N., Bacman, S.R., Plastini, M.J. & Moraes, C.T. The mitochondrial DNA polymerase gamma degrades linear DNA fragments precluding the formation of deletions. *Nat Commun* **9**, 2491 (2018).
8. Mottis, A., Herzig, S. & Auwerx, J. Mitocellular communication: Shaping health and disease. *Science* **366**, 827-832 (2019).
9. Butow, R.A. & Avadhani, N.G. Mitochondrial signaling: the retrograde response. *Mol Cell* **14**, 1-15 (2004).
10. Shpilka, T. & Haynes, C.M. The mitochondrial UPR: mechanisms, physiological functions and implications in ageing. *Nat Rev Mol Cell Biol* **19**, 109-120 (2018).
11. Eckl, E.M., Ziegemann, O., Krumwiede, L., Fessler, E. & Jae, L.T. Sensing, signaling and surviving mitochondrial stress. *Cell Mol Life Sci* **78**, 5925-5951 (2021).
12. Costa-Mattioli, M. & Walter, P. The integrated stress response: From mechanism to disease. *Science* **368** (2020).
13. Bahat, A., MacVicar, T. & Langer, T. Metabolism and Innate Immunity Meet at the Mitochondria. *Front Cell Dev Biol* **9**, 720490 (2021).
14. Tigano, M., Vargas, D.C., Tremblay-Belzile, S., Fu, Y. & Sfeir, A. Nuclear sensing of breaks in mitochondrial DNA enhances immune surveillance. *Nature* **591**, 477-481 (2021).
15. Kim, J. *et al.* VDAC oligomers form mitochondrial pores to release mtDNA fragments and promote lupus-like disease. *Science* **366**, 1531-1536 (2019).
16. Dhir, A. *et al.* Mitochondrial double-stranded RNA triggers antiviral signalling in humans. *Nature* **560**, 238-242 (2018).
17. Yu, C.H. *et al.* TDP-43 Triggers Mitochondrial DNA Release via mPTP to Activate cGAS/STING in ALS. *Cell* **183**, 636-649 e618 (2020).
18. Zhong, Z. *et al.* New mitochondrial DNA synthesis enables NLRP3 inflammasome activation. *Nature* **560**, 198-203 (2018).
19. Fessler, E. *et al.* A pathway coordinated by DELE1 relays mitochondrial stress to the cytosol. *Nature* **579**, 433-437 (2020).
20. Guo, X. *et al.* Mitochondrial stress is relayed to the cytosol by an OMA1-DELE1-HRI pathway. *Nature* **579**, 427-432 (2020).
21. Bayona-Bafaluy, M.P., Blits, B., Battersby, B.J., Shoubridge, E.A. & Moraes, C.T. Rapid directional shift of mitochondrial DNA heteroplasmy in animal tissues by a mitochondrially targeted restriction endonuclease. *Proc Natl Acad Sci U S A* **102**, 14392-14397 (2005).
22. Moretton, A. *et al.* Selective mitochondrial DNA degradation following double-strand breaks. *PLoS One* **12**, e0176795 (2017).

23. Orlowski, J. & Bujnicki, J.M. Structural and evolutionary classification of Type II restriction enzymes based on theoretical and experimental analyses. *Nucleic Acids Res* **36**, 3552-3569 (2008).
24. Ong, S.E. & Mann, M. A practical recipe for stable isotope labeling by amino acids in cell culture (SILAC). *Nature protocols* **1**, 2650-2660 (2006).
25. Kim, D.I. *et al.* An improved smaller biotin ligase for BioID proximity labeling. *Mol Biol Cell* **27**, 1188-1196 (2016).
26. Cox, J. & Mann, M. MaxQuant enables high peptide identification rates, individualized p.p.b.-range mass accuracies and proteome-wide protein quantification. *Nat Biotechnol* **26**, 1367-1372 (2008).
27. Rath, S. *et al.* MitoCarta3.0: an updated mitochondrial proteome now with sub-organelle localization and pathway annotations. *Nucleic Acids Res* **49**, D1541-D1547 (2021).
28. Han, S. *et al.* Proximity Biotinylation as a Method for Mapping Proteins Associated with mtDNA in Living Cells. *Cell Chem Biol* **24**, 404-414 (2017).
29. Gilkerson, R. *et al.* The mitochondrial nucleoid: integrating mitochondrial DNA into cellular homeostasis. *Cold Spring Harb Perspect Biol* **5**, a011080 (2013).
30. Xavier, V.J. & Martinou, J.C. RNA Granules in the Mitochondria and Their Organization under Mitochondrial Stresses. *Int J Mol Sci* **22** (2021).
31. Leonetti, M.D., Sekine, S., Kamiyama, D., Weissman, J.S. & Huang, B. A scalable strategy for high-throughput GFP tagging of endogenous human proteins. *Proc Natl Acad Sci U S A* **113**, E3501-3508 (2016).
32. Shibata, Y. *et al.* Mechanisms determining the morphology of the peripheral ER. *Cell* **143**, 774-788 (2010).
33. Branda, S.S. *et al.* Yeast and human frataxin are processed to mature form in two sequential steps by the mitochondrial processing peptidase. *J Biol Chem* **274**, 22763-22769 (1999).
34. Nabhan, J.F., Gooch, R.L., Piatnitski Chekler, E.L., Pierce, B. & Bulawa, C.E. Perturbation of cellular proteostasis networks identifies pathways that modulate precursor and intermediate but not mature levels of frataxin. *Sci Rep* **5**, 18251 (2015).
35. Anderson, N.S. & Haynes, C.M. Folding the Mitochondrial UPR into the Integrated Stress Response. *Trends Cell Biol* **30**, 428-439 (2020).
36. Fessler, E., Krumwiede, L. & Jae, L.T. DELE1 tracks perturbed protein import and processing in human mitochondria. *Nat Commun* **13**, 1853 (2022).
37. Sidrauski, C. *et al.* Pharmacological dimerization and activation of the exchange factor eIF2B antagonizes the integrated stress response. *Elife* **4**, e07314 (2015).
38. Tsai, J.C. *et al.* Structure of the nucleotide exchange factor eIF2B reveals mechanism of memory-enhancing molecule. *Science* **359** (2018).
39. Zyryanova, A.F. *et al.* Binding of ISRIB reveals a regulatory site in the nucleotide exchange factor eIF2B. *Science* **359**, 1533-1536 (2018).
40. Wong, Y.C., Ysselstein, D. & Krainc, D. Mitochondria-lysosome contacts regulate mitochondrial fission via RAB7 GTP hydrolysis. *Nature* **554**, 382-386 (2018).
41. Gilquin, B. *et al.* The AAA+ ATPase ATAD3A controls mitochondrial dynamics at the interface of the inner and outer membranes. *Mol Cell Biol* **30**, 1984-1996 (2010).
42. Gross, N.J., Getz, G.S. & Rabinowitz, M. Apparent turnover of mitochondrial deoxyribonucleic acid and mitochondrial phospholipids in the tissues of the rat. *J Biol Chem* **244**, 1552-1562 (1969).
43. Shokolenko, I., Venediktova, N., Bochkareva, A., Wilson, G.L. & Alexeyev, M.F. Oxidative stress induces degradation of mitochondrial DNA. *Nucleic Acids Res* **37**, 2539-2548 (2009).
44. Suter, M. & Richter, C. Fragmented mitochondrial DNA is the predominant carrier of oxidized DNA bases. *Biochemistry* **38**, 459-464 (1999).

45. Horvath, S.E. *et al.* Role of membrane contact sites in protein import into mitochondria. *Protein Sci* **24**, 277-297 (2015).
46. Shammas, M.K. *et al.* OMA1 mediates local and global stress responses against protein misfolding in CHCHD10 mitochondrial myopathy. *J Clin Invest* **132** (2022).
47. Stephan, T., Roesch, A., Riedel, D. & Jakobs, S. Live-cell STED nanoscopy of mitochondrial cristae. *Sci Rep* **9**, 12419 (2019).
48. Arbustini, E. *et al.* Mitochondrial DNA mutations and mitochondrial abnormalities in dilated cardiomyopathy. *Am J Pathol* **153**, 1501-1510 (1998).
49. Arguello, T. *et al.* ATAD3A has a scaffolding role regulating mitochondria inner membrane structure and protein assembly. *Cell Rep* **37**, 110139 (2021).
50. He, J. *et al.* Mitochondrial nucleoid interacting proteins support mitochondrial protein synthesis. *Nucleic Acids Res* **40**, 6109-6121 (2012).
51. Peralta, S. *et al.* ATAD3 controls mitochondrial cristae structure in mouse muscle, influencing mtDNA replication and cholesterol levels. *J Cell Sci* **131** (2018).
52. Zhao, Y. *et al.* ATAD3A oligomerization causes neurodegeneration by coupling mitochondrial fragmentation and bioenergetics defects. *Nat Commun* **10**, 1371 (2019).
53. Trifunovic, A. *et al.* Premature ageing in mice expressing defective mitochondrial DNA polymerase. *Nature* **429**, 417-423 (2004).
54. Nicholls, T.J. *et al.* Linear mtDNA fragments and unusual mtDNA rearrangements associated with pathological deficiency of MGME1 exonuclease. *Hum Mol Genet* **23**, 6147-6162 (2014).
55. Wall, C.E. *et al.* High-fat diet and FGF21 cooperatively promote aerobic thermogenesis in mtDNA mutator mice. *Proc Natl Acad Sci U S A* **112**, 8714-8719 (2015).
56. Forsstrom, S. *et al.* Fibroblast Growth Factor 21 Drives Dynamics of Local and Systemic Stress Responses in Mitochondrial Myopathy with mtDNA Deletions. *Cell Metab* **30**, 1040-1054 e1047 (2019).
57. Khan, N.A. *et al.* mTORC1 Regulates Mitochondrial Integrated Stress Response and Mitochondrial Myopathy Progression. *Cell Metab* **26**, 419-428 e415 (2017).

Extended Data Figures:

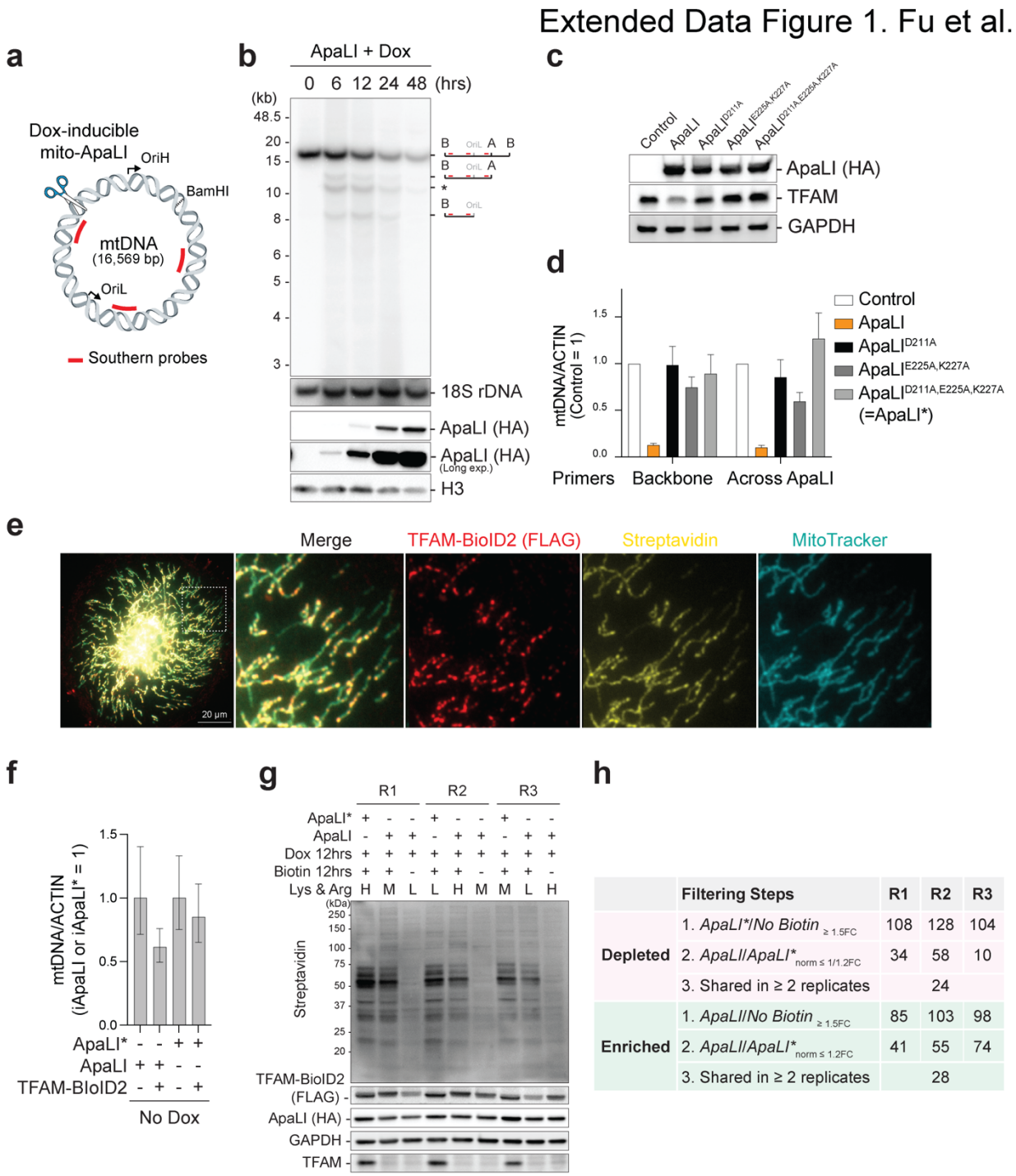

	Filtering Steps	R1	R2	R3
Depleted	1. *ApaLI*/No Biotin* $_{\geq 1.5FC}$	108	128	104
	2. *ApaLI/ApaLI** $_{norm \leq 1/1.2FC}$	34	58	10
	3. Shared in ≥ 2 replicates		24	
Enriched	1. *ApaLI/No Biotin* $_{\geq 1.5FC}$	85	103	98
	2. *ApaLI/ApaLI** $_{norm \leq 1.2FC}$	41	55	74
	3. Shared in ≥ 2 replicates		28	

Extended Data Fig. 1 | Establishing a TFAM-BioID2 based proteomic approach to identify proteins in the vicinity of nucleoids. a, Schematic of mtDSB formation using a mitochondria-

localized restriction enzyme ApaLI that is controlled by a doxycycline (Dox) inducible promoter. Depicted in red are probes that were used in southern blot and recognizing different mtDNA regions. Extracted mtDNA was linearized with BamHI. **b**, Southern blot analysis of mtDNA and nuclear 18S rDNA (loading control) in cells with the indicated treatment. Western blot analysis of ApaLI (anti-HA) and histone H3 (loading control). A, ApaLI; B, BamHI; (*) depicts a degradation intermediate with unknown end points. Long exp., long exposure of Western blot. **c**, Western blot analysis of ApaLI (anti-HA) and TFAM in 293T cells transfected with wildtype and catalytically inactive ApaLI for two days. Cells transfected with a GFP plasmid served as a control. **d**, mtDNA copy number in 293T cells with the indicated treatments as in **c**, measured by qPCR of ND2 ("Backbone") and 12S (region "Across ApaLI") relative to ACTIN. All samples were normalized to control cells transfected with a GFP plasmid. **e**, Representative image of immunofluorescence of TFAM-BioID2 (anti-FLAG) and biotinylated proteins (streptavidin) in ARPE-19 cells expressing TFAM-BioID2 and treated with 50 nM biotin for 12 hours. **f**, mtDNA copy number in cells expressing TFAM-BioID2 and ApaLI or ApaLI*. mtDNA content measured by qPCR of the 12S (mtDNA) and normalized to ACTIN locus. mtDNA levels in cells expressing TFAM-BioID2 was normalized to control cells lacking TFAM-BioID2. Normalized copy numbers in Extended Data Fig. 1d and f are means ± s.d. from n = 3 technical replicates. **g**, Western blot analysis of protein biotinylation (streptavidin), TFAM-BioID2 (anti-FLAG) and ApaLI (anti-HA) in cell lysates prior to pooling for streptavidin pull-down and mass spectrometry. Replicates: R1, R2, R3. Lys, lysine; Arg, arginine; H, heavy; M, medium; L, light. **h**, Filtering steps to highlight proteins that were depleted and enriched in cells expressing ApaLI versus ApaLI*. FC, fold change; norm, SILAC ratio normalized to TFAM-BioID2.

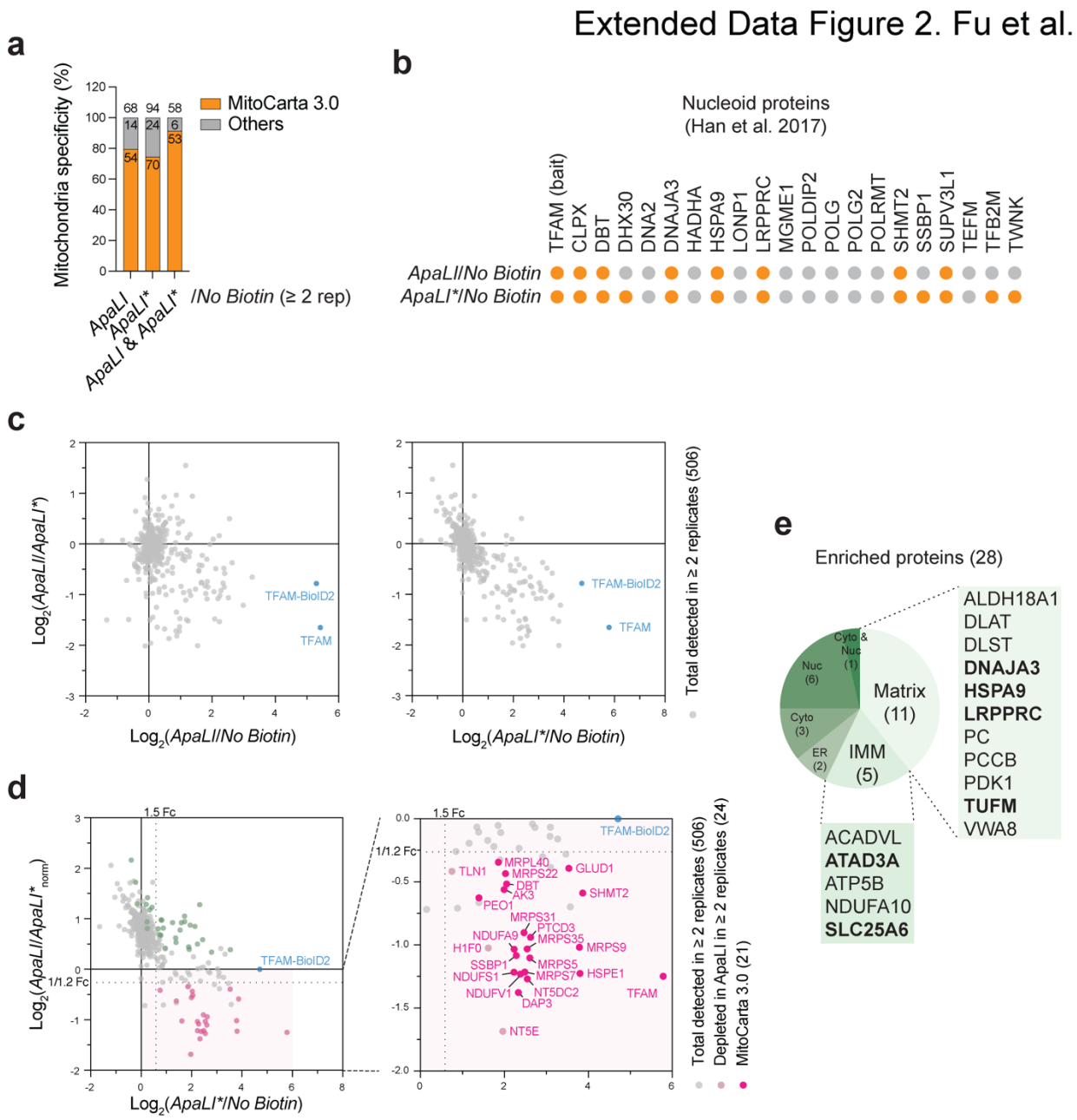

Extended Data Fig. 2 | BioID-based proteomic analysis reveals changes in nucleoid composition in response to mtDSBs. a, Percentage of mitochondrial proteins defined by MitoCarta 3.0 among all proteins captured by TFAM-BioID2. TFAM-BioID2 captured proteins pass Filtering Step 1 in Fig. 1e (≥ 1.5 fold change of *ApaLI*/*No Biotin* or *ApaLI**/*No Biotin* SILAC ratio) and are present in ≥ 2 replicates. Protein numbers are indicated on the bars. *ApaLI* & *ApaLI**, proteins shared between *ApaLI* and *ApaLI**. **b**, Nucleoid proteins detected among TFAM-BioID2 captured proteins are labeled in orange. A list of 21 nucleoid proteins was curated in Han et al.

2017[1]. **c**, SILAC ratio plot showing the log2(*ApaLI*/*ApaLI**) against log2(*ApaLI*/*No Biotin*) or log2(*ApaLI**/*No Biotin*). TFAM-BioID2 SILAC ratios were calculated based on peptides from BioID2. **d**, SILAC ratio plot showing normalized log2(*ApaLI*/*ApaLI**) against log2(*ApaLI**/*No Biotin*). 24 proteins depleted in *ApaLI* are highlighted in pink. Among them, 21 MitoCarta 3.0 proteins are marked in dark pink on the right. **e**, Categories of subcellular localization of 28 mtDSB-enriched proteins with names listed for those from mitochondrial matrix and inner membrane (IMM). Proteins in bold were tested in Extended Data Fig. 7b.

Extended Data Figure 3. Fu et al.

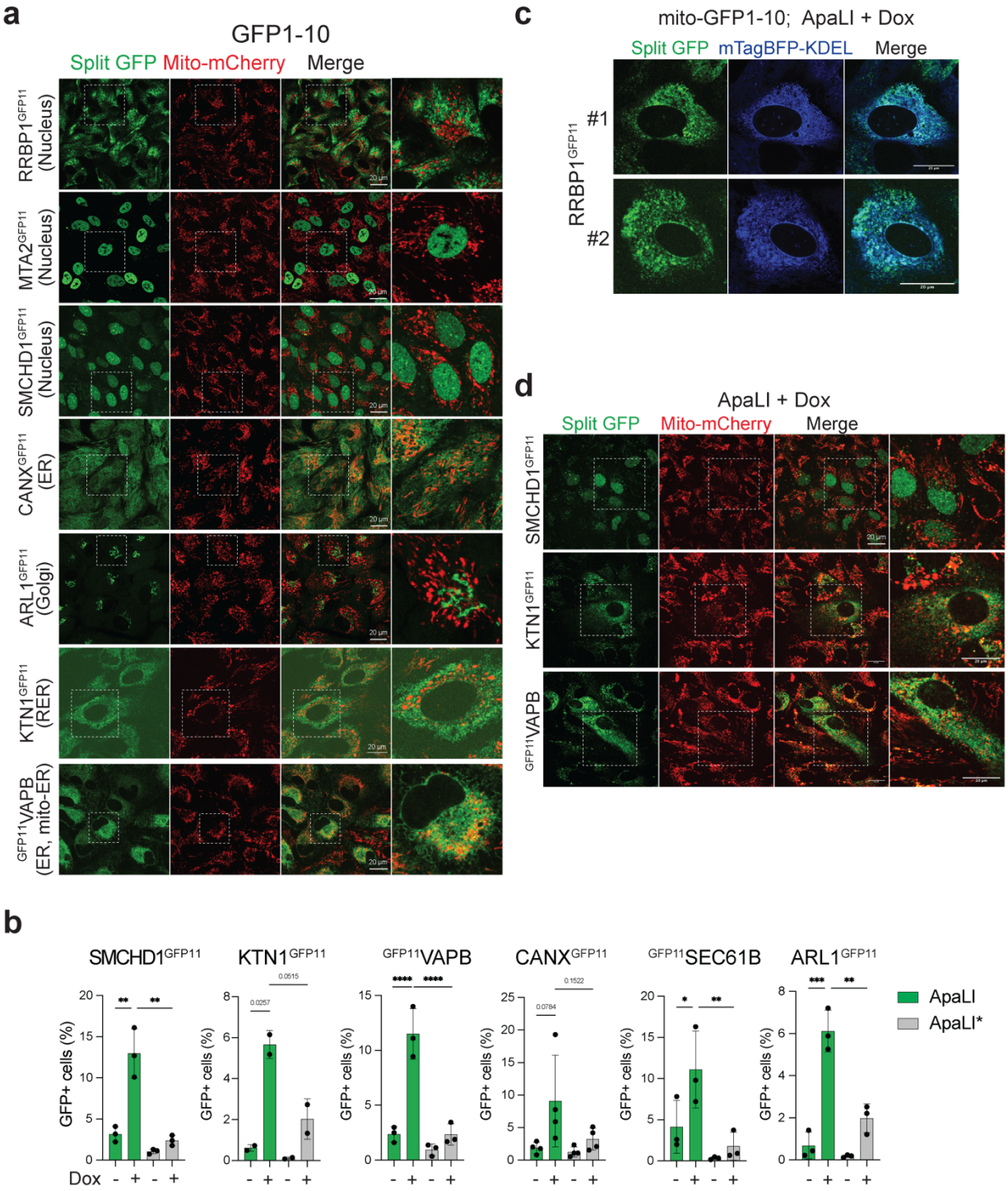

Extended Data Fig. 3 | Mis-localization of mitochondria-targeted GFP1-10 upon mtDSBs. a, Representative images of reconstituted split GFP in cells with the indicated proteins endogenously tagged with GFP11, and GFP1-10 (without MLS) expressed in cytosol. In these

experiments, expression of non-mitochondrial localized GFP1-10 was used to confirm the proper GFP11 targeting of the indicated genes. Expected localization of the protein being tagged is indicated in parenthesis. RER, rough ER; mito-ER, mitochondria-ER contact site. Scale bar, 20 μm. **b**, Flow cytometry analysis of GFP+ percentage in cells expressing mito-GFP1-10 and GFP11-tagged SMCHD1 ($SMCHD1^{GFP11}$), KTN1 ($KTN1^{GFP11}$), VAPB ($^{GFP11}VAPB$), CANX ($CANX^{GFP11}$), SEC61B ($^{GFP11}SEC61B$), or ARL ($ARL1^{GFP11}$) under mtDSBs. GFP11 tagged cells expressing ApaLI and ApaLI* were treated with Dox for 2 days. Data are means ± s.d. of n = 3 to 4 biological replicates; one-way ANOVA. $^{*}P \leq 0.05$, $^{**}P \leq 0.01$, $^{***}P \leq 0.001$, $^{****}P \leq 0.0001$. **c**, Representative image of reconstituted split GFP co-localized with the ER network, labeled with mTagBFP-KDEL, in $RRBP1^{GFP11}$ cells expressing mito-GFP1-10 and ApaLI, and treated with Dox for 2 days. Scale bar, 20 μm. **d**, Representative images of cellular localization of reconstituted split GFP in $SMCHD1^{GFP11}$, $KTN1^{GFP11}$, and $^{GFP11}VAPB$ cells 2 days post-Dox induction of ApaLI. Scale bar, 20 μm.

Extended Data Figure 4. Fu et al.

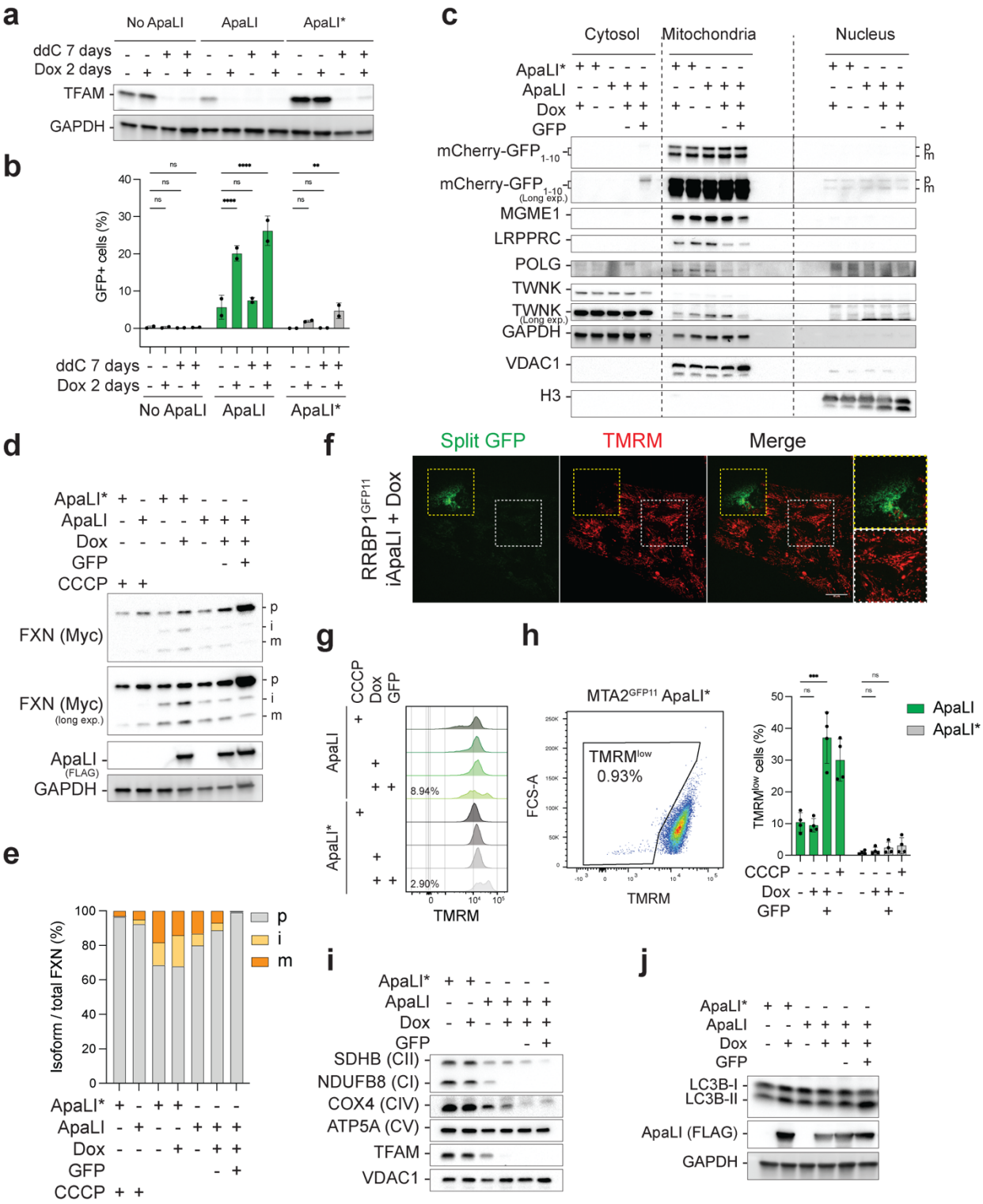

Extended Data Fig. 4 | Impaired mitochondria function in response to mtDNA breaks. a, Western blot analysis of TFAM in MTA2^{GFP11} cells expressing ApaLI, ApaLI*, and no ApaLI, and

treated with Dox and/or ddC. **b**, Percentage of GFP+ cells determined by flow cytometry in cells as per Extended Data Fig. 4a. Data are means ± s.d. of *n* = 2 biological replicates; two-way ANOVA. **c**, Subcellular fractionation followed by Western blot analysis of indicated proteins on MTA2^{GFP11} cells with indicated treatments, including cell sorting based on GFP. p, precursor isoform; m, mature isoform; Long exp., long exposure of Western blots. **d**, Western blot analysis of three isoforms of frataxin (FXN) transfected to GFP- and GFP+ populations of MTA2^{GFP11} cells expressing ApaLI and treated with Dox for 2 days. Mitochondrial uncoupler CCCP (Carbonyl cyanide *m*-chlorophenyl hydrazone) was used at 20 μM for 6 hours. i, intermediate isoform. **e**, Western blot quantification of frataxin isoforms in Extended Data Fig. 4d, normalized to the total level of all isoforms. **f**, Representative image of TMRM (Tetramethylrhodamine, methyl ester) staining in RRBP1^{GFP11} cells expressing mito-GFP1-10 and ApaLI and treated with Dox for 2 days. Yellow and white boxes depict examples of GFP+ and GFP- cells, respectively. **g-h**, Flow cytometry analysis of TMRM staining in RRBP1^{GFP11} cells expressing mito-GFP1-10 and ApaLI (or ApaLI*). Analysis was carried out 2 days post-Dox treatment. **g**, Representative histograms generated from FlowJo software showing TMRM intensity on the X-axis, unit area on the Y-axis; the frequencies of GFP+ cells are labeled. **h**, Percentage of cells with low TMRM signal (TMRM^{low} cells) gated based on untreated ApaLI* cells (left). Data are means ± s.d. of *n* = 4 biological replicates; two-way ANOVA. *$P \leq 0.05$, **$P \leq 0.01$, ***$P \leq 0.001$, ****$P \leq 0.0001$. **i**, Western blot analysis of nucleus-encoded OXPHOS proteins in the mitochondrial fraction of GFP- and GFP+ populations from MTA2^{GFP11} cells expressing ApaLI and treated with Dox for 2 days. **j**, Western blot analysis of LC3B-I/II in sorted GFP+ population of Dox-treated MTA2^{GFP11} cells expressing ApaLI.

Extended Data Figure 5. Fu et al.

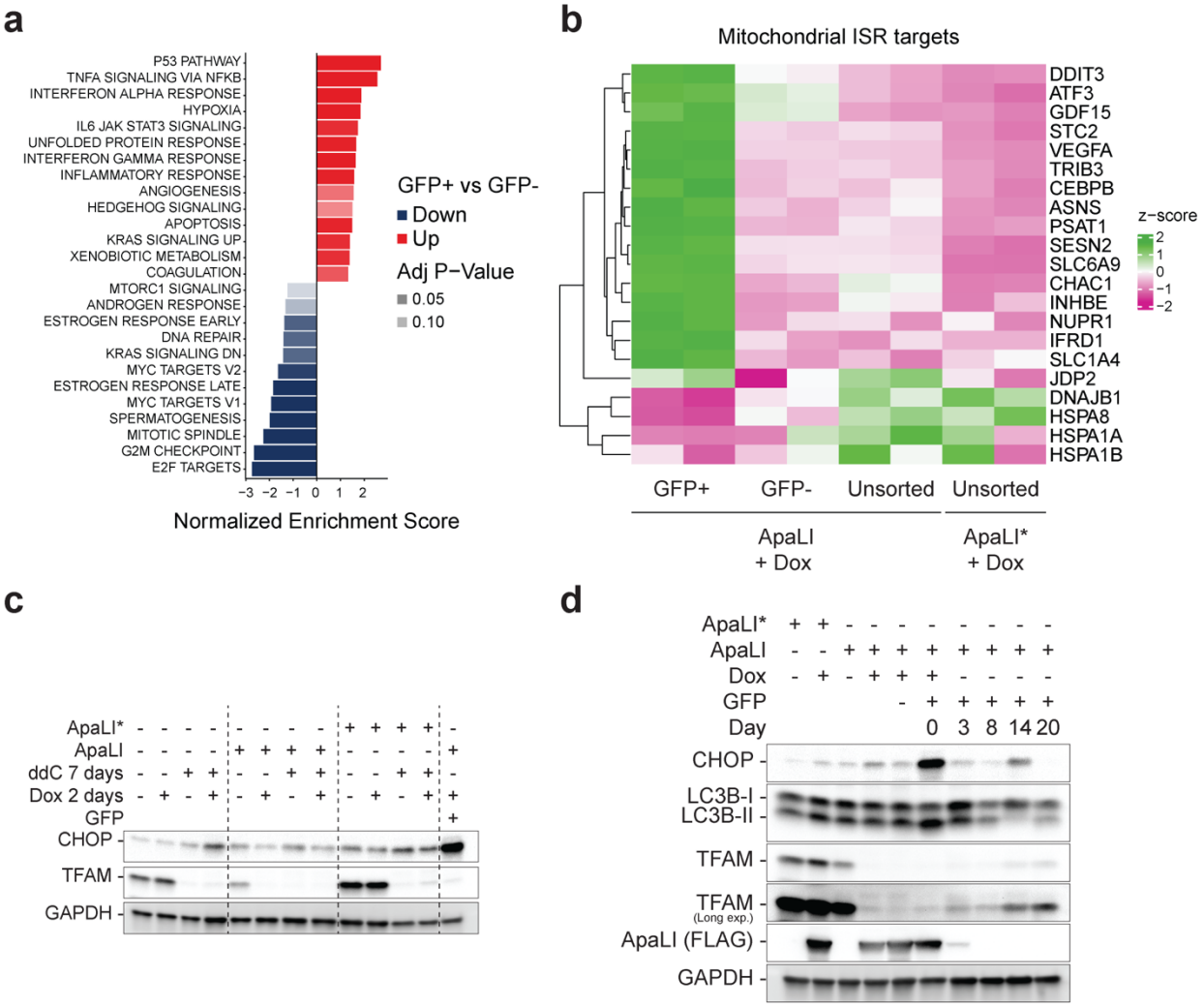

Extended Data Fig. 5 | Acute activation of the integrated stress response in a subset of cells under mtDSBs. a, Gene Set Enrichment Analysis of differentially expressed genes in GFP+ vs. GFP- MTA2^{GFP11} cells induced with Dox for ApaLI expression (2 fold change, adjusted p-value < 0.01, 2 replicates) using MSigDB hallmark gene sets. Red bars indicating up-regulated pathways and blue bars representing down-regulated genes in GFP+ cells. **b**, Heatmap of ISR target gene expression (according to Fessler, et al. Nature. 2020.[2]) in GFP- and GFP+ populations of MTA2^{GFP11} cells expressing ApaLI (or ApaLI*) and treated with Dox for 2 days. Two replicates per condition. **c**, Western blot analysis of CHOP in MTA2^{GFP11} cells expressing ApaLI, or ApaLI*. Cells were treated with Dox and/or ddC. Sorted GFP+ population from MTA2^{GFP11} cells under mtDSBs served as a positive control. **d**, Western blot analysis of CHOP, LC3B-I/II and TFAM in

sorted GFP+ population of Dox-treated MTA2^{GFP11} cells expressing ApaLI. Dox was removed post cell sorting on Day 0.

Extended Data Figure 6. Fu et al.

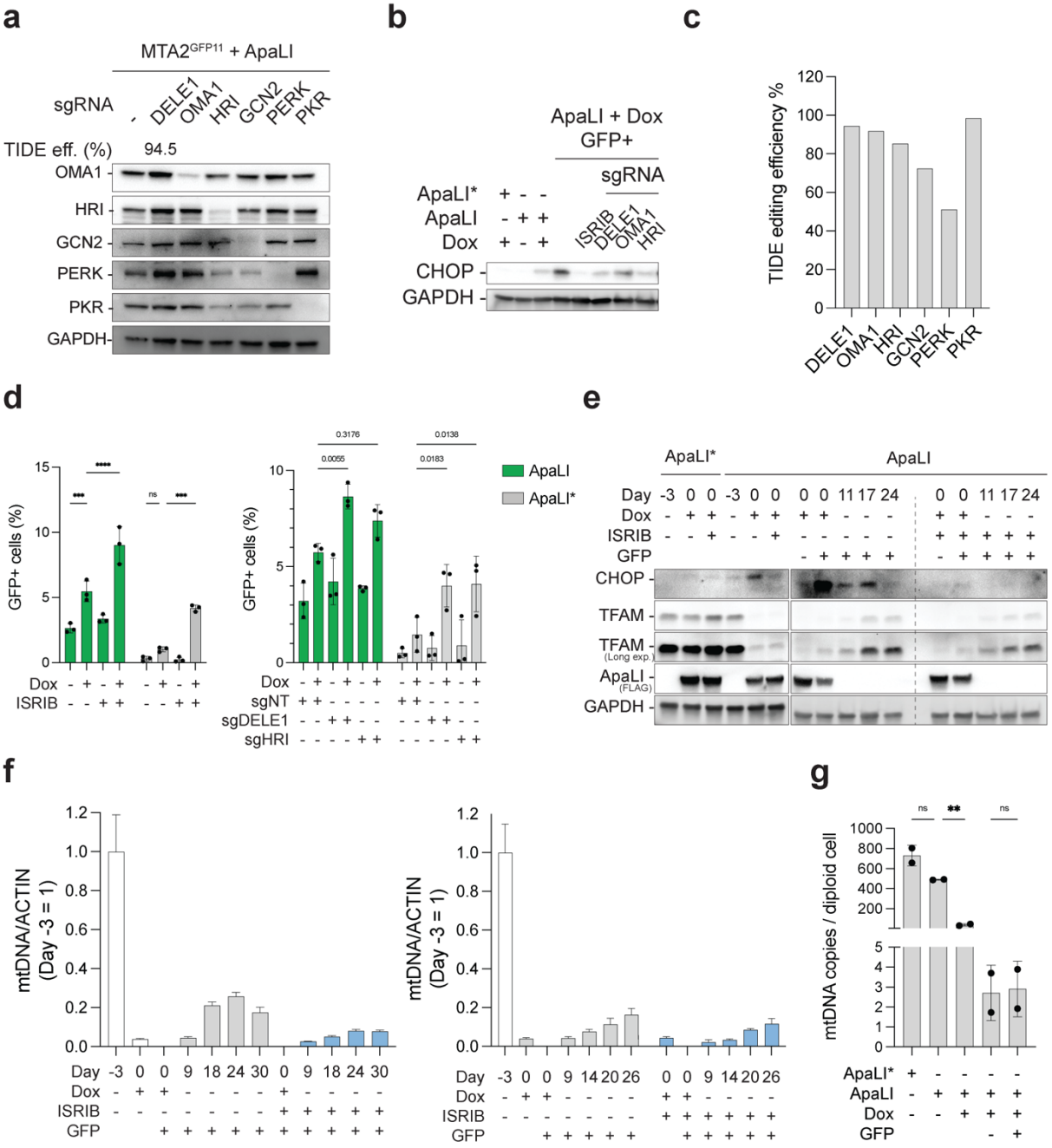

Extended Data Fig. 6 | OMA1 – DELE1 – HRI triggers an acute ISR upon mtDSBs to re-establish mitochondrial function. a, CRISPR/Cas9 editing efficiency of DELE1 determined by TIDE and OMA1, HRI, GCN2, PERK and PRK assessed by Western blots in MTA2^{GFP11} cells expressing ApaLI used in Fig 4a. **b**, Western blot analysis of CHOP in the GFP+ population of MTA2^{GFP11} cells subjected to mtDSBs and indicated treatments. **c**, CRISPR/Cas9 editing efficiency in samples represented in Fig. 4b, analyzed by TIDE. **d**, Flow cytometry analysis of GFP+ cell percentage in Dox-induced MTA2^{GFP11} cells expressing ApaLI, or ApaLI* and subjected to indicated treatments: ISRIB and CRISPR knock-out of DELE1. sgNT, non-targeted sgRNA. Data are means ± s.d. of $n = 3$ biological replicates; two-way ANOVA. ***$P \leq 0.001$, ****$P \leq 0.0001$. **e**, Western blot analysis of CHOP and TFAM for samples in Fig. 4c. **f**, Copy number dynamics of mtDNA in sorted GFP+ populations of MTA2^{GFP11} cells that are under mtDSBs with and without ISRIB treatment. MTA2^{GFP11} cells expressing ApaLI were treated with Dox at Day -3 and Dox was withdrawn at Day 0. Values at different time points were normalized to Day -3. Two repetition experiments of Fig. 4c. **g**, mtDNA copy number per cell in sorted GFP- versus GFP+ populations of MTA2^{GFP11} cells under mtDSBs, quantified by digital droplet PCR. Data are means ± s.d. of $n = 2$ biological replicates. One-way ANOVA. **$P \leq 0.01$.

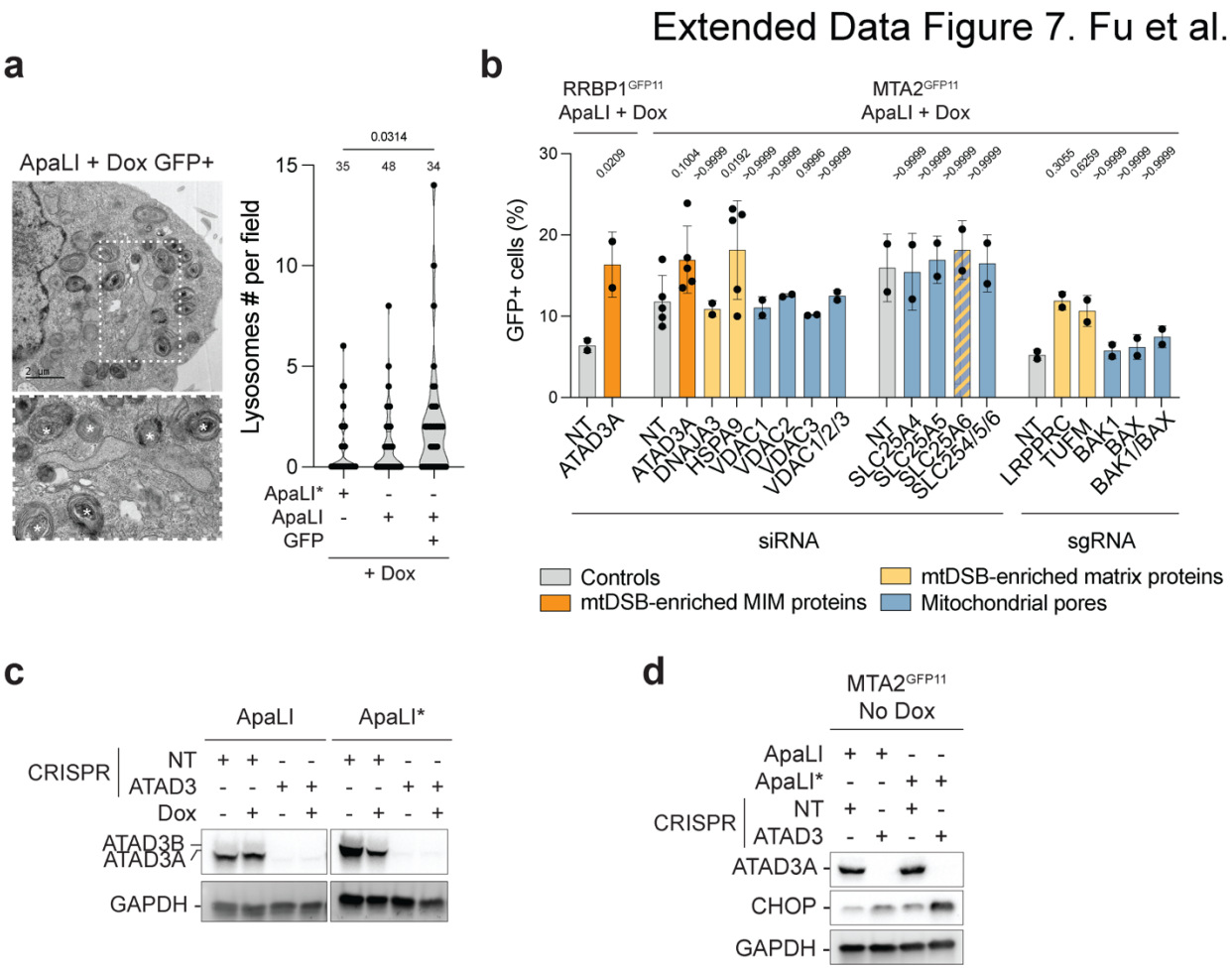

Extended Data Fig. 7 | Defective cristae in cells subjected to mtDNA damage. a, Violin plot presenting lysosome numbers per field. Lysosome examples were marked by (*) in the representative image from GFP+ ApaLI-induced cells. Numbers of fields analyzed for each sample is labeled above the violins. Two-way ANOVA. **b**, Percentage of GFP positive cells determined by flow cytometry analysis in MTA2^{GFP11}, or RRBP1^{GFP11} cells that were expressing Dox-induced ApaLI for 2 days and subjected to siRNA or CRISPR perturbation of genes as indicated. Data are means ± s.d. of *n* = 2-4 biological replicates; two-way ANOVA. P-values indicated were calculated by comparing to corresponding controls. **c**, Western blots analysis of ATAD3A/B in MTA2^{GFP11} cells treated with sgRNA targeting ATAD3. **d**, Western blots analysis of CHOP in MTA2^{GFP11} cells treated with sgRNA targeting ATAD3.

Extended Data Table 1 | SILAC mass spectrometry results of TFAM-BioID2 associated proteins in response to mtDSBs.

Extended Data Table 2 | Oligos used in this paper, including primers for qPCR and PCR, CRISPR/Cas9 editing gRNAs and donors, etc.

Extended Data Table 3 | Antibodies and dilutions used in Western Blots of this paper.

Extended Data Video 1 | Electron tomogram of mitochondria in MTA2^{GFP11} cells with ApaLI* induced for 2 days.

Extended Data Video 2 | Electron tomogram of mitochondria in MTA2^{GFP11} cells with ApaLI induced for 2 days.

Extended Data Video 3 | Electron tomogram of mitochondria in GFP+ MTA2^{GFP11} cells with ApaLI induced for 2 days.

Extended Data Video 4 | 3D reconstructed mitochondria in MTA2^{GFP11} cells with ApaLI* induced for 2 days.

Extended Data Video 5 | 3D reconstructed mitochondria in MTA2^{GFP11} cells with ApaLI induced for 2 days.

Methods:

Plasmids

mito-ApaLI (pcDNA3-ApaLI-HA)[3] was generously provided by Carlos Moraes. The catalytically inactive mutants of ApaLI, ApaLI^{D211A}, ApaLI^{E225A,K227A}, and ApaLI^{D211A,E225A,K227A}, were generated through overlapping PCR using primers harboring the desired mutations. Doxycycline-inducible ApaLI and ApaLI* plasmids used in Fig. 1, and Extended Data Fig. 1-2 (lenti-TRE3G-ApaLI(*)-Hygro) were cloned into LT3REVIR (Addgene Plasmid #111176) by inserting mito-ApaLI(*) (HA-tagged) after a Tet-On 3G promoter and adding Hygromycin selection marker. The doxycycline-inducible ApaLI(*) plasmid (TLCV2-ApaLI(*)-T2A-mTagBFP2-Puro) used in all other figures were cloned using the all-in-one Dox-inducible lentiviral backbone of TLCV2 (Addgene Plasmid #97360) by inserting mito-ApaLI(*) (FLAG-tagged) after the Tet-responsive promoter (TRE), with an addition of a T2A-mTagBFP fragment in-frame with mito-ApaLI(*).

The TFAM-BioID2 fusion plasmid (lenti-CMV-TFAM-BioID2-IRES-Puro) was cloned by first inserting TFAM cDNA into the backbone of MCS-BioID2-HA[4] (Addgene Plasmid #74224) with the addition of a short linker (2xGGGGS) between TFAM and BioID2. The region containing CMV promoter and TFAM-BioID2 was then cloned into a lentiviral vector that includes Puromycin selection marker.

The lentiviral mito-mCherry-GFP1-10 plasmid (pHAGE2-EF1a-F0ATPMLS-mCherry-GFP1-10) was created by cloning the mitochondria-localized mCherry-GFP1-10 region from plasmid MTS-mCherry-GFP1-10-Hyg-N1[5] (Addgene Plasmid #91957) into a lentiviral backbone with an EF-1α promoter driving the expression. For TMRM staining (Extended Data Fig. 4g,h), mCherry was removed from the mito-mCherry-GFP1-10 plasmid by cloning. GFP1-10 plasmid (pHAGE2-EF1a-GFP1-10-IRES-Puro) was generated by cloning GFP1-10 from pcDNA3.1-GFP(1-10) (Addgene Plasmid #70219) into a lentiviral vector that contains EF-1α promoter and Puromycin selection marker. The lentiviral BFP-KDEL plasmid (pHAGE2-EF1a-BFP-KDEL-IRES-Hygro) was based on BFP-KDEL (Addgene Plasmid #49150). Frataxin plasmid (pCMV6-FXN-Myc-FLAG) was purchased from Origene (RC204880). The lentiviral 4xGFP11-SEC61B plasmid (pHAGEF2-EF1a-4xGFP11-SEC61B-IRES-Hygro) was generated by cloning SEC61B from mCherry-SEC61B (Addgene Plasmid #121160), adding 4xGFP11 fragment in-frame to its 5' end, and inserting the entire 4xGFP11-SEC61B fragment into a lentiviral vector that contains EF-1α promoter and Hygromycin selection marker.

Cell culture procedures and treatment

All cells were grown in an incubator at 5% CO_2 and 37°C. ARPE-19 cells (ATCC CRL-2302) were immortalized with hTERT. ARPE-19 cells and 293T cells (ATCC CRL-3216) used for lentiviral production are cultured in Dulbecco's modified Eagle medium (DMEM, Corning, 10-013-CV) supplemented with 10% Bovine Calf Serum (GeminiBio), 2 mM L-glutamine (Gibco), 100 U/ml Penicillin-Streptomycin (Gibco), 0.1 mM MEM non-essential amino acids (Gibco), and 50 ug/ml uridine (Sigma-Aldrich). Prior to introduction of dox-inducible ApaLI (or ApaLI*) by transfection or lentiviral transduction, cells were switched to be cultured in Dulbecco's modified Eagle medium (DMEM, Corning, 10-013-CV) supplemented with 10% tetracycline-free fetal bovine serum (FBS, TaKaRa Cat. #631368), 2 mM L-glutamine (Gibco), 100 U/ml Penicillin-Streptomycin (Gibco), 0.1 mM MEM non-essential amino acids (Gibco), and 50 µg/ml uridine (Sigma-Aldrich).

All lentiviral productions were done by transfecting 293T cells with equal amount of lentiviral packaging combo (pMDLg/pRRE (Addgene Plasmid #12251), pRSV-Rev (Addgene Plasmid #12253), VSV-G (pMD2.G, Addgene Plasmid #12259) in 1:1:1 molar ratio), and plasmid of interest, and changing to fresh media 12 hours post-transfection. Supernatant of 293T cells containing fresh lentivirus was collected every 24 hours after media change and applied to cells to be infected.

ApaLI and ApaLI* was induced with 1 µg/ml doxycycline (Dox). For mtDNA depletion, 20 µM ddC was added for 5 days prior to Dox treatment with a total of 7 days of ddC treatment. For ISR inhibition, ISRIB was added to cells at 200 nM for at least 12 hours prior to ApaLI induction. To induce apoptosis, cells were co-treated with 1µM ABT-737 and 1µM S63845 for 3 hours before collection.

Proximity-based protein biotinlyation and streptavidin pull-down

ARPE-19 cells were transduced with lenti-TRE3G-ApaLI(*)-Hygro lentivirus and selected with 300 µg/ml Hygromycin. Due to high heterogeneity of ApaLI(*) expression among cells after Dox induction, we picked clonal cells that were confirmed with 100% ApaLI(*) induction efficiency by immunofluorescence (IF). Two clones (named ApaLI and ApaLI* in Fig. 1, and Extended Data Fig. 1-2) with comparable expression of ApaLI and ApaLI* upon Dox treatment were chosen for TFAM-BioID2 introduction. ApaLI and ApaLI* cells were transduced with relatively low level of

TFAM-BioID2 lentivirus and selected with 1 μg/ml Puromycin. Proper TFAM-BioID2 localization and biotinylation were confirmed by IF after treating the cells with 50 nM biotin.

To metabolically label the proteomes of TFAM-BioID expressing ApaLI(*) cells with heavy (H), medium (M) or light (L) isotopes of lysine and arginine, we cultured each cell line in three 6 cm plates starting from 10% confluency. One plate was cultured in light SILAC media: DMEM deficient in L-lysine and L-arginine (DMEM for SILAC, Thermo Fisher, A33822) supplemented with 84 mg/ml L-arginine (Arg0) and 146 mg/ml L-lysine (Lys0) (Sigma-Aldrich), 10% dialyzed fetal bovine serum (Gibco), 100 U/ml Penicillin-Streptomycin (Gibco), 0.1 mM MEM non-essential amino acids (Gibco), and 50 ug/ml Uridine (Sigma-Aldrich). The second plate was cultured in medium SILAC media with the same composition as above except Arg0 and Lys0 were replaced by L-Arginine [$^{13}C_6$] HCl (Arg-6) and L-ysine-4,4,5,5-d_4 (Lys-4) (Cambridge Isotope Laboratories). The third plate was cultured in heavy SILAC media with the same composition except arginine and lysine were replaced by L-Arginine [$^{13}C_6$,D_7,$^{15}N_4$]HCl (Arg-17) and L-Lysine [$^{13}C_6$,$^{15}N_2$]HCl (Lys-8) (Cambridge Isotope Laboratories). Cells were passaged and expanded in the corresponding SILAC media for 10 doublings.

Each replicate is comprised of three conditions: *No Biotin* (ApaLI treated with Dox), *ApaLI* (ApaLI treated with Dox and biotin), and *ApaLI** (ApaLI* treated with Dox and biotin) (Fig. 1e). Within the same replicate, each condition utilized cells labeled in different SILAC media. Each condition across different replicates also used cells labeled in different SILAC media (Extended Data Fig. 1g). In short, the design of conditions in three replicates with different SILAC isotopes is as follow: Replicate 1, *No Biotin* (L), *ApaLI* (M), *ApaLI** (H); Replicate 2, *No Biotin* (M), *ApaLI* (H), *ApaLI** (M); Replicate 3, *No Biotin* (M), *ApaLI* (H), *ApaLI** (M). 40 million cells were plated in 4 15-cm plates for each condition in each replicate. For biotinylation and ApaLI activation, 50 nM biotin and 1 μg/ml doxycycline were added to the media simultaneously for 12 hours.

Cell lysis and streptavidin pull-down procedures were done as Step 34-41 in Hung et al. Nature Protocol. 2016[6], with mild modifications as follow. Cell pellets of 40 million cells were lysed in freshly prepared 800 μl of RIPA buffer (50 mM Tris, 150 mM NaCl, 0.1% SDS, 0.5% sodium deoxycholate, 1% Triton X-100, 1x Halt Protease and Phosphatase Inhibitor Cocktail (Thermo Fisher), 1 mM PMSF, 10 mM sodium azide, and 10 mM sodium ascorbate) and rotating at 4°C for 30 minutes. Lysates were clarified by centrifugation at 15,000 x *g* for 10 minutes at 4°C. Protein concentration in the supernatant was measured using the Pierce BCA protein assay kit (Thermo Fisher). Whole-cell lysates (5 mg of protein) from the H, M, L samples of the same replicate were

mixed in a 1:1:1 H:M:L ratio by protein mass. 15 mg of lysate mixtures were incubated with 1.875 ml streptavidin magnetic beads (Dynabeads MyOne Streptavidin C1, Thermo Fisher, 65001) slurry that were pre-washed with RIPA buffer twice. The suspensions were incubated at 4°C overnight with gentle rotation. Streptavidin beads were then washed twice with 2 ml RIPA buffer, twice with 2M urea in 10 mM Tris-HCl pH 8.0, and again twice with 2 ml RIPA buffer, and twice with 50 mM Tris-HCl pH7.4, 50 mM NaCl. Biotinylated proteins were eluted by incubating the beads with 225 µl Laemmli buffer (4% (w/v) SDS, 20% glycerol, 120 mM Tris-HCl, pH6.8) supplemented with 20 mM DTT and 2 mM biotin, and heating to 95°C for 5 minutes.

Protein digestion and extraction

Proteins were reduced with 2.5 µl 0.2 M dithiothreitol (Sigma) for one hour at 57 ºC at pH 7.5. Subsequently samples were alkylated with 2.5 µl 0.5 M iodoacetamide (Sigma) for 45 minutes at room temperature in the dark. NuPAGE LDS Sample buffer (1X) (Invitrogen) was added to the samples and the samples transferred to a NuPAGE 4-12% Bis-Tris Gel 1.0 mm x 10 well (Invitrogen) for SDS PAGE gel electrophoresis. The gel was stained with GelCode Blue Stain Reagent (Thermo Scientific). Sample lanes were excised and destained with 1:1 (v/v) methanol and 100 mM ammonium bicarbonate at 4°C with agitation. Destained gel pieces were dehydrated in a SpeedVac concentrator. Dried gel pieces were resuspended in 300 µL 100 mM ammonium bicarbonate with 250 ng Promega trypsin for overnight digestion. A 300 µL solution of 5% formic acid and 0.2% trifluoroacetic acid (TFA) R2 50 µm Poros (Applied Biosystems) beads slurry in water was added to the gel pieces before returning the samples to the shaker for an additional three hours at 4°C. Beads were loaded onto equilibrated C18 ziptips (Millipore), with 0.1% TFA, using a microcentrifuge for 30 seconds at 6,000 rpm. The beads were washed with 0.5% acetic acid. Peptides were eluted with 40% acetonitrile in 0.5% acetic acid followed by 80% acetonitrile in 0.5% acetic acid. The organic solvent was removed using a SpeedVac concentrator. The samples were reconstituted in 0.5% acetic acid and stored at -80°C until analysis.

Liquid chromatography (LC) – mass spectrometry (MS)

LC separation was performed online on EASY-nLC 1000 (Thermo Scientific) utilizing Acclaim PepMap 100 (75 um x 2 cm) precolumn and PepMap RSLC C18 (2 um, 100A x 50 cm) analytical column. Peptides were gradient eluted from the column directly to Orbitrap Q Exactive HF-X mass spectrometer using a 215 min acetonitrile gradient from 5 to 26 % B in 179 min followed by ramp to 40% B in 20 min and final equilibration in 100% B for 15 min (A=2% ACN

0.5% AcOH / B=80% ACN 0.5% AcOH). Flow rate was set at 200 nl/min. High resolution full MS spectra were acquired with a resolution of 45,000, an AGC target of 3e6, with a maximum ion injection time of 45 ms, and scan range of 400 to 1500 m/z. Following each full MS scan 20 data-dependent HCD MS/MS scans were acquired at the resolution of 15,000, AGC target of 1e5, maximum ion time of 120 ms, one microscan, 2 m/z isolation window, NCE of 27, fixed first mass 150 m/z and dynamic exclusion for 30 seconds. Both MS and MS^2 spectra were recorded in profile mode.

Analysis to determine the differential proteins in response to mtDSBs

MS data were analyzed using MaxQuant software version 1.6.3.4[7] and searched against the SwissProt subset of the human uniprot database (http://www.uniprot.org/) containing 20,430 entries with sequences for ApaLI and BioID2 appended. Database search was performed in Andromeda[8] integrated in MaxQuant environment. A list of 248 common laboratory contaminants included in MaxQuant was also added to the database as well as reversed versions of all sequences. For searching, the enzyme specificity was set to trypsin with the maximum number of missed cleavages set to 2. The precursor mass tolerance was set to 20 ppm for the first search used for non-linear mass re-calibration[9] and then to 6 ppm for the main search. Oxidation of methionine was searched as variable modification; carbamidomethylation of cysteines was searched as a fixed modification. SILAC labeling with 3 channels (referred as SILAC ratio) were used as a quantification option. The false discovery rate (FDR) for peptide, protein, and site identification was set to 1%, the minimum peptide length was set to 6.

Only proteins with quantified SILAC ratios across all conditions (*ApaLI*/*No Biotin*, *ApaLI**/*No Biotin*, *ApaLI*/*ApaLI**) and in ≥ 2 replicates were retained for analysis. We noticed that TFAM-BioID2 (quantified using peptides assigned to BioID2) was reduced in *ApaLI* compared to *ApaLI** due to mtDNA degradation after DSBs, similar to TFAM (including endogenous TFAM, and TFAM from TFAM-BioID2 overexpression) (Extended Data Fig. 2c). Given that decreased level of TFAM-BioID2 bait likely leads to reduction in protein biotinylation, we normalized the *ApaLI*/*ApaLI** SILAC ratio of all proteins to that of TFAM-BioID2.

Proteins depleted upon mtDSBs were regarded as enriched in *ApaLI** compared to *ApaLI*. We first ensured proteins captured by TFAM-BioID2 in *ApaLI** are above background, using a cut-off of *ApaLI**/*No Biotin* ≥ 1.5 (Extended Data Fig. 1h, Depleted Step 1). Next, we retrieved proteins

depleted upon mtDSBs using criteria normalized *ApaLI*/*ApaLI** ≤ 1/1.2 and shared in ≥ 2 replicates (Extended Data Fig. 1h, Depleted Step 2-3).

For proteins enriched upon mtDSBs, we first identified proteins captured by TFAM-BioID2 in *ApaLI* as above background, using a cut-off of *ApaLI*/*No Biotin* ≥ 1.5 (Extended Data Fig. 1h, Enriched Step 1). Next, we retrieved proteins enriched upon mtDSBs using criteria normalized *ApaLI*/*ApaLI** ≥ 1.2 and shared in ≥ 2 replicates (Extended Data Fig. 1h, Enriched Step 2-3).

Western blot analysis

Cells harvested were counted and lysed in 10 µl Laemmli buffer (4% (w/v) SDS, 20% glycerol, 120 mM Tris-HCl, pH6.8) per 100,000 cells. Lysates were vortexed and boiled at 95°C for 10 minutes. Proteins from equivalent numbers of cells were then separated by SDS-PAGE and transferred to a nitrocellulose or PVDF membrane using Trans-Blot Turbo Transfer System or Mini Trans-blot cells (Bio-Rad). Membranes were blocked in 5% milk in TBST (137 mM NaCl, 2.7 mM KCl, 19 mM Tris Base, 0.1% Tween-20) or 5% BSA in TBST for p-eIF1α for 1 hour, followed by incubation with primary antibodies in 1% milk (1% BSA for p-eIF1α) overnight at 4°C. Subsequently, membranes were washed with TBST 3 times, incubated with HRP-linked secondary antibodies at 1:2,500 dilution and washed again. Membranes were then developed with Clarity Western ECL Substrate (Bio-Rad) and imaged on ChemiDoc XRS+ Imager (Bio-Rad). Loading control GAPDH was detected by a Rhodamine conjugated antibody against GAPDH. Full list of antibodies and their dilutions used in the study is available in Extended Table 3.

Genomic DNA isolation

Purified total genomic DNA was used for mtDNA copy number measurement by qPCR and southern blot. Cell pellets harvested were resuspended in 400 µl PBS buffer containing 0.2% (w/v) SDS, 5 mM EDTA, and 0.2 mg/ml Proteinase K, and incubated at 50°C for 6 hours with constant shaking at 1,000 rpm. DNA was precipitated by adding 0.3 M Sodium Acetate, pH5.2 and 600 µl isopropanol and being kept at -20°C for over 2 hours. Precipitated DNA was centrifuged at 20,000 x *g* at 4°C for 30 minutes, followed by 70% ethanol wash. DNA was then resuspended in TE buffer (10 mM Tris-HCl, pH8.0, 0.1 mM EDTA) and quantified by Nanodrop.

mtDNA copy number

To determine relative mtDNA copy number by qPCR, sequences specific to mtDNA (ND2, 12S) and the nuclear ACTIN locus (Supplementary Table 2) were independently amplified from 12.5 ng of total genomic DNA with ssoAdvanced SYBR Green Supermix (Bio-Rad) in a total volume of 10 µl with standard cycling condition suggested by Bio-Rad. qPCR reactions were run on Roche LightCycler 480 or Applied Biosystems QuantStudio 6 Real-Time PCR System. In the LightCycler 480 software, basic relative quantification method was used with mtDNA as target and ACTIN as reference. In the QuantStudio 6 software, Comparative C_T experiment was used with ACTIN being the endogenous control.

To determine absolute mtDNA copy number by digital droplet PCR, we followed the ddMDM method (O'Hara, et al. Genome Research. 2019) for cell lysis. Following Proteinase K treatment, samples were diluted with ddH_2O 1:125 to obtain the final concentration of 10 cell equivalents per µl. 1 µL cell lysate was combined with locus-specific primers, FAM-labeled MT-ND4 (mtDNA) and HEX-labeled EIF2C (nuclear DNA) probes (Extended Table 2), Hind III, and digital PCR Supermix for probes (no dUTP). Cycling conditions for the probes were tested to ensure optimal annealing/extension temperature as well as optimal separation of positive from empty droplets. Optimization was done with a known positive control. All reactions were performed on a QX200 ddPCR system (Bio-Rad catalog # 1864001) and each sample was evaluated in technical duplicates or triplicates. Reactions were partitioned into a median of ~10,000 droplets per well using the QX200 droplet generator. Emulsified PCRs were run on a 96-well thermal cycler using cycling conditions identified during the optimization step (95°C 10 seconds; 40 cycles of 94°C 30 seconds and 54, 56, or 60°C 1 second; 98°C 10 seconds; 4°C hold). Plates were read and analyzed with the QuantaSoft software to assess the number of droplets positive for gene of interest, reference gene, both, or neither. mtDNA copy numbers per cell were calculated as follow: MT-ND4 droplet number / EIF2C droplet number * 2.

Southern blot

Purified genomic DNA was digested with BamHI-HF restriction enzyme (NEB) at 5 units per 1 µg DNA, for 6 hours at 37°C. Products, along with Quick-Load 1kb Extend DNA Ladder (NEB) were separated on a 0.6% agarose gel supplemented with ethidium bromide at 30 V for 24 hours at 4°C. The ladders were imaged on ChemiDoc XRS+ Imager (Bio-Rad) before blotting. The agarose gels went through the following washes: 1) depurination (0.25 M HCl) for 30 minutes, 2) twice denaturation (1.5 M NaCl, 0.5 M NaOH) for 30 minutes, 3) twice neutralization (3M NaCl, 0.5 M Tris-HCl, pH7.0) for 30 minutes. The gels were blotted to Amersham Hybond-N membranes

(GE) via overnight capillary transfer with 20x SSC (3M NaCl, 0.3 M sodium citrate). The membranes were crosslinked under UV at 1200x100 μJ/cm^2 and then incubated in pre-hybridization buffer (1.5x SSC, 1% SDS, 7.5% dextran sulphate and 125 μg/ml salmon sperm DNA) at 65°C for 1 hour. Probes specific for human mtDNA were PCR amplified from 3 regions as in Moretton, et al. PLOS ONE. 2017[10], and probes specific for nuclear 18S ribosomal DNA were amplified using primers as in Peeva, et al. Nature Communications. 2018[11]. For probe labeling, 75 ng of each of purified PCR products was mixed with 1 μl Random Hexamers (50 μM, Invitrogen) in a total volume of 30 μl, which was then boiled at 95°C for 5 minutes and cooled to room temperature. The reaction was supplemented with 1 μl DNA Ploymerase I, Large (Klenow) fragment (NEB), 5 μl dCTP [α-32P] (3000Ci/mmol), 1x NEBuffer 2 and 33 μM dATP, dGTP, dTTP, and incubated at RT for 90 minutes. After adding 50 μl TNES buffer (20 mM EDTA, 400 mM NaCl, 0.5% SDS, 50 mM Tris base), reactions were deactivated at 65°C for 10 minutes. Probes were then purified through a Sephadex G-50 fine (GE) column made with TNE buffer (50 mM Tris-HCl, pH7.4, 100 mM NaCl, 0.1 mM EDTA) in a 3 ml syringe. Eluted probes (in 1 ml TNES buffer) were boiled at 95°C for 5 minutes and immediately added to the membrane in pre-hybridization buffer. After overnight hybridization at 65°C, membranes were washed once with 4x SSC, three times with 2x SSC supplemented with 0.1% SDS, and wrapped and exposed to storage phosphor screens, which were scanned using Typhoon Imager (GE).

Immunofluorescence (IF)

ARPE-19 cells expressing TFAM-BioID2 were plated on coverslips in 6-well plates and treated with 50 nM biotin for 12 hours. Cells were stained with 125 nM MitoTracker Deep Red (Invitrogen) for 30 minutes. Cells were rinsed with PBS buffer and fixed with 4% paraformaldehyde for 10 minutes at RT. After PBS washes, cells were permeabilized with 0.5% Triton X-100 in PBS buffer for 10 minutes at RT, followed by PBS washes. Cells on coverslips were blocked with blocking buffer (1 mg/ml BSA, 3% goat serum, 0.1% Triton X-100, 1mM EDTA) for 30 minutes at RT, and incubated with FLAG antibody (Sigma F3165, 1:10000) and Alex Fluor 488 conjugated Streptavidin (Invitrogen S11223, 1:2000) in blocking buffer overnight at 4°C. Cells were then washed with PBS, hybridized with Alexa Fluor 594 conjugated anti-mouse secondary antibody for 1 hour at RT. After PBS washes and DAPI staining, coverslips were mounted on glass slides with ProLong Gold Antifade mountant (Invitrogen). Slides were imaged on a Nikon ECLIPSE Ei2-E inverted microscope.

Tagging of endogenous proteins and gene knock out by CRISPR/Cas9

For tagging of genes of interest with GFP11, the CRISPR ribonucleoprotein (RNP) complex of gRNA and Cas9 protein (IDT), together with a single-stranded donor (ssODN) were delivered into mito-GFP1-10 cells using the Nucleofector system (Lonza). Cell line constitutively expressing mito-mCherry-GFP1-10 was generated by transducing ARPE-19 cells with lentiviral mito-mCherry-GFP1-10 and enriched for mCherry positive cells via cell sorting. gRNAs were designed close to the stop codon of the genes (and start codon of VAPB). 500 nt ssODNs containing MYC and 4xGFP11 flanked by ~100 nt homology arms and mutated PAMs (protospacer adjacent motif) were ordered from IDT. Full list of gRNA targets and ssODNs used in the study is available in Extended Table 2. RNP complexes preparation was based on IDT protocol, by 1) annealing equal amount of 100 μM Alt-R CRISPR-Cas9 crRNA and 100 μM tracrRNA to form gRNA, and 2) incubating 150 pmol gRNA with 125 pmol Alt-R Cas9 enzyme for 20 minutes. 5 μl RNP complex, 1.5 μg ssODN and 1.2 μl 100 μM Alt-R Cas9 Electroporation Enhancer (IDT) were mixed and added to 20,000 cells resuspended in 18 μl SF Nucleofection Buffer (Lonza). Nucleofection mixture were transferred to 16-well Nucleocuvette strips (Lonza) and nucleofected with the 4D-Nucleofector X unit (Lonza) using ER-100 program. After recovered in 100 μl RPMI 1640 media (Gibco) for 10 minutes, cells were plated in prewarmed culture media supplemented with 1 μM Alt-R HDR Enhancer V2 (IDT). After 48-72 hours, cells were plated at clonal density in 15 cm plates for clonal cell isolation. Colonies were screened by genotyping PCR using primers flanking the editing site (outside of homology arm regions) and looking for larger PCR products potentially containing GFP11 insertion. Clonal cells with potential homozygous or heterozygous knock-in were chosen and further confirmed by transducing GFP1-10 without MLS and detecting GFP signal at the primary localization of the protein (e.g. ER for RRBP1, VAPB, KTN1; golgi for ARL1). Confirmed clones were introduced with ApaLI and ApaLI* by lentiviral transduction to examine GFP signal upon mtDSBs. For GFP11 tagging of SEC61B, the ARPE-19 cell line expressing mito-mCherry-GFP1-10 was transduced with lentiviral 4xGFP11-SEC61B and selected for integration using Hygromycin. Confirmation of proper localization of SEC61B and introduction of ApaLI and ApaLI* were done in the same way as above for cells knocked in with GFP11.

Gene knock-outs followed the same procedure of CRISPR RNP delivery, excluding ssODN and HDR enhancer. For Fig 4a, $MTA2^{GFP11}$ cells were nucleofected with CRISPR RNP. Knock-out efficiencies were mostly confirmed by Western blots, except that DELE1, which has no available antibody[12], was confirmed by PCR (Extended Table 2) and TIDE analysis (https://tide.nki.nl). $MTA2^{GFP11}$ cells with ISR factor depletion were expanded and transduced with ApaLI. Cells were then induced with Dox and sorted for GFP+ cells for downstream Western blot analysis. For Fig

4b, 5e and Extended Fig 6a,b,7b,c, MTA2^{GFP11} cells expressing ApaLI (and ApaLI*) were nucleofected with CRISPR RNP. 48 hours after CRISPR delivery, cells were induced with Dox and analyzed by flow cytometry or Western blots.

Flow cytometry

For flow cytometry analysis of split GFP signal, GFP11 tagged cells expressing Dox-induced ApaLI or ApaLI* (-T2A-mTagBFP) were trypsinized, centrifuged, resuspended in 3% FBS in PBS and passed through cell strainers. Cells were analyzed on LSR Fortessa analyzer (BD) with GFP signal detected through 488 nm laser and 525/50 Bandpass (BP) filter, mCherry detected through 561 nm laser and 610/20 BP filter, mTagBFP detected through 405 nm laser and 450/50 BP filter. Recorded data was analyzed using FlowJo software. After gating for singlet living cells, mTagBFP negative populations were gated for samples without Dox induction, and mTagBFP positive cells were gated for samples with Dox induced. Subsequently, GFP+ populations were gated based on ApaLI* without Dox treatment and the same gating was applied across all samples.

Live cell imaging by spinning disk confocal microscope

All imaging on split GFP signal was performed at live cell imaging condition. Cells were plated on glass bottom plates (Cellvis) and induced with Dox. Prior to imaging, media was changed to live cell imaging media (DMEM, high glucose, HEPES, no phenol red (Gibco, 21063029) supplemented with 10% Bovine Calf Serum (GeminiBio), 2 mM L-glutamine (Gibco), 100 U/ml Penicillin-Streptomycin (Gibco), 0.1 mM MEM non-essential amino acids (Gibco), and 50 ug/ml uridine (Sigma-Aldrich)). Cells were imaged on Nikon CSU-W1 Spinning Disk Confocal microscope with 100x oil lens. TOKAI HIT STX system was used to maintain cells at 37°C, 5% CO_2 and humidity. Within every experiment, laser percentage and exposure time for each channel were set the same across all samples in comparison. Captured images were then analyzed on Fiji software by setting the same minimum and maximum intensity for samples in comparison.

Incucyte growth analysis

MTA2^{GFP11} cells expressing ApaLI and ApaLI* were induced with Dox for 48 hours. MTA2^{GFP11} cells with ApaLI induction were sorted for GFP- and GFP+ populations by flow cytometry. After overnight recovery of the sorted cells, 12,000 cells from each condition were plated in duplicates in 48-well plates containing Dox-free media. Plates were imaged every 24 hours on the Incucyte S3 Live-cell analysis system (Sartorius) using brightfield and 10x objective and capturing 16 fields

per well. Cell confluency was measured using Incucyte analysis software with settings as follow: 0.5 Segmentation Adjustment, 700 μm^2 Hole Fill, 2000 μm^2 minimal area.

Subcellular fractionation

Cells were harvested and processed using Cell Fractionation Kit (Abcam ab109719) following standard protocol with optimization for ARPE-19 cells. 50 µl 1x Buffer A and 50 µl Buffer B (or Buffer C) were used for 500,000 cells. Buffer B was prepared by diluting Detergent I 500-fold in 1x Buffer A. Buffer C was prepared by diluting Detergent II 12.5-fold in 1x Buffer A. Cytosol and mitochondrial extractions were both done on a rotator for 30 minutes at RT. All centrifugation steps during extraction were done for 5 minutes at 4°C.

Frataxin transfection

$MTA2^{GFP11}$ cells expressing ApaLI and ApaLI* were induced with Dox for 48 hours. $MTA2^{GFP11}$ cells with ApaLI induction were sorted for GFP- and GFP+ populations by flow cytometry. 350,00 cells per sample were seeded in a 6-well to recover overnight. Cells were transfected with 0.5 µg frataxin plasmid using Lipofectamine 3000 (Invitrogen) and 36 hours later harvested for Western blot analysis. Treatment of 20 µM CCCP was done 6 hours prior to harvesting.

TMRM staining and analysis

ARPE-19 cells were CRISPR/Cas9 targeted to introduce 4xGFP11 to the C-terminal of RRBP. Confirmed homozygous clone was transduced with mito-GFP1-10 (without mCherry), followed by transduction of ApaLI and ApaLI*. Cells were plated in glass-bottom plates (Cellvis). After induced with Dox for 2 days, cells were stained with 1 µM TMRM (Invitrogen) in culture media for 30 minutes at 37°C. Subsequently media was replaced with live cell imaging media as indicated in Live cell imaging. For flow cytometry analysis of TMRM signal, cells after staining were trypsinized, centrifuged and resuspended in 3% FBS in PBS. Cells were analyzed on LSR Fortessa analyzer. TMRM signal was detected through 561 nm laser and 586/15 Bandpass filter. Recorded data was analyzed using FlowJo software. $TMRM^{low}$ gating was set based on TMRM-stained ApaLI* cells and was applied to all conditions, including GFP+ and GFP- subpopulations. As a positive control, ApaLI and ApaLI* cells were treated with 20 µM CCCP for 6 hours. While ApaLI* cells without Dox induction were resistant to CCCP, ApaLI* cells were sensitive to membrane potential loss upon CCCP treatment.

RNA sequencing (RNA-seq) and analysis

Four conditions were prepared for the RRBP1^{GFP11} (or MTA2^{GFP11}) cell line: 1) ApaLI* treated with Dox (unsorted), and 2) unsorted, 3) GFP- subset, 4) GFP+ subset of ApaLI treated with Dox, with two replicates for each condition. For each sample, 500,000 cells were harvested as a pellet and kept frozen at -80°C before handing over to the Integrated Genomics Operation at MSKCC for RNA purification, TruSeq stranded mRNA (polyA) library preparation and sequencing.

Frozen cells were lysed in 1 ml TRIzol Reagent (Thermo Fisher 15596018) and phase separation was induced with 200 µl chloroform. RNA was extracted from 350 µl of the aqueous phase using the miRNeasy Mini Kit (Qiagen 217004) on the QIAcube Connect (Qiagen) according to the manufacturer's protocol. Samples were eluted in 33 µl RNase-free water. After RiboGreen quantification and quality control by Agilent BioAnalyzer, 500 ng of total RNA with RIN values of 8.9 - 10 underwent polyA selection and TruSeq library preparation according to instructions provided by Illumina (TruSeq Stranded mRNA LT Kit, RS-122-2102), with 8 cycles of PCR. Samples were barcoded and run on a NovaSeq 6000 in a PE100 run, using the NovaSeq 6000 S4 Reagent Kit (200 Cycles) (Illumina). An average of 45 million paired reads was generated per sample. The percent of mRNA bases averaged 91%.

RNA-seq data was analyzed using an automated pipeline Seq-N-Slide (10.5281/zenodo.5550459.) designed to work on the BigPurple HPC cluster at NYU Langone Health. RNA-seq analysis of the Seq-N-Slide pipeline used STAR (Spliced Transcripts Alignment to a Reference) for alignment, DESeq2 for differential gene expression analysis, and GSEA (Gene Set Enrichmen Analysis) for pathway analysis.

Heatmaps in Fig. 3a,d, Extended Data Fig. 5b present the z-scores of individual genes, which were calculated by applying regularized log (`rlog()`) and scaling (`scale()`, across all 8 samples) functions to the `.rds` file derived from DESeq2 analysis. The list of mitochondrial ISR target genes used in Fig. 3d and Extended Data Fig 5b was obtained from Fessler, et al. Nature. 2020 [2] and is composed of ATF4, CHOP target genes and heat shock protein genes that are induced by CCCP and are dependent on DELE1–HRI–eIF2α signaling.

Transmission electron microscopy and analysis

Cultured cells were fixed in 0.1 M sodium cacodylate buffer (pH 7.4) containing 2.5% glutaraldehyde and 2% paraformaldehyde for 2 hours and post-fixed with 1% osmium tetroxide

and 1% potassium ferrocyanide for one hour at 4ºC, then block stained in 0.25% aqueous uranyl acetate, processed in a standard manner and embedded in EMbed 812 (Electron Microscopy Sciences, Hatfield, PA). 70 nm ultrathin sections were cut (UC6 microtome; Leica Microsystems) and mounted on 200 mesh copper grids. 200 nm thickness sections were collected on slotted copper grids (Electron Microscopy Sciences, Hatfield, PA) coated with formvar membrane. All sections were counterstained by incubation with 3% uranyl acetate in 50% methanol for 20 min, followed by washing in water, and incubation with Renyld's lead citrate for 5 min.

For Fig. 5a,b and Extended Data Fig. 7a,70 nm ultrathin sections were imaged under Talos120C transmission electron microscope (Thermo Fisher Scientific) with Gatan (4k x 4k) OneView Camera (Gatan, Inc., Pleasanton, CA). 30-50 fields per sample were randomly imaged at 8000x magnification for statistical analysis. For cristae morphology quantification, mitochondria sections with paralleled and lamellar cristae were considered as "normal", and mitochondria sections without paralleled and lamellar cristae, including complete loss of cristae, were considered as "missing/aberrant" cristae morphology.

200 nm thickness sections were used for tomogram in Fig. 5c and Extended Data Video. 1-5. In detail, 10 nm gold particles were put on grids as fiducial marker before a thin layer of carbon (Auto306 Vacuum Evaporator; Edwards BOC) was evaporated on top of 200 nm sections to minimize beam-induced specimen shrinkage during data collection for tomograms. Samples were imaged with JEOL 1400 Flash TEM (JEOL Ltd.) equipped with Gatan Rio16 camera at 8,000X nominal magnification (corresponding to a 1.27-nm pixel size) and 2.1 μm defocus. Dual-axis tilt series were collected with a dual-axis tomography holder (Model 2040, Fischione Instruments) using a tilt range of ± 65° with a 2° increment (SerialEM 3.0). To collect the tilt series about the second axis the sample was rotated 90° using the holder's sample rotation mechanism, and the same region reimaged. Fiducial alignment of projection images and calculation of 3-D volumes was carried out using Protomo software (Winkler and Taylor,2006) and creation of dual-axis reconstruction was done in IMOD[13, 14]. Reconstructions were manually segmented in ORS Dragonfly (The Objects) after applying a 3 × 3 × 3 median filter.

References:

1. Han, S. *et al.* Proximity Biotinylation as a Method for Mapping Proteins Associated with mtDNA in Living Cells. *Cell Chem Biol* **24**, 404-414 (2017).

2. Fessler, E. *et al.* A pathway coordinated by DELE1 relays mitochondrial stress to the cytosol. *Nature* **579**, 433-437 (2020).
3. Bayona-Bafaluy, M.P., Blits, B., Battersby, B.J., Shoubridge, E.A. & Moraes, C.T. Rapid directional shift of mitochondrial DNA heteroplasmy in animal tissues by a mitochondrially targeted restriction endonuclease. *Proc Natl Acad Sci U S A* **102**, 14392-14397 (2005).
4. Kim, D.I. *et al.* An improved smaller biotin ligase for BioID proximity labeling. *Mol Biol Cell* **27**, 1188-1196 (2016).
5. Ruan, L. *et al.* Cytosolic proteostasis through importing of misfolded proteins into mitochondria. *Nature* **543**, 443-446 (2017).
6. Hung, V. *et al.* Spatially resolved proteomic mapping in living cells with the engineered peroxidase APEX2. *Nature protocols* **11**, 456-475 (2016).
7. Cox, J. & Mann, M. MaxQuant enables high peptide identification rates, individualized p.p.b.-range mass accuracies and proteome-wide protein quantification. *Nat Biotechnol* **26**, 1367-1372 (2008).
8. Cox, J. *et al.* Andromeda: a peptide search engine integrated into the MaxQuant environment. *J Proteome Res* **10**, 1794-1805 (2011).
9. Cox, J., Michalski, A. & Mann, M. Software lock mass by two-dimensional minimization of peptide mass errors. *J Am Soc Mass Spectrom* **22**, 1373-1380 (2011).
10. Moretton, A. *et al.* Selective mitochondrial DNA degradation following double-strand breaks. *PLoS One* **12**, e0176795 (2017).
11. Peeva, V. *et al.* Linear mitochondrial DNA is rapidly degraded by components of the replication machinery. *Nat Commun* **9**, 1727 (2018).
12. Guo, X. *et al.* Mitochondrial stress is relayed to the cytosol by an OMA1-DELE1-HRI pathway. *Nature* **579**, 427-432 (2020).
13. Kremer, J.R., Mastronarde, D.N. & McIntosh, J.R. Computer visualization of three-dimensional image data using IMOD. *J Struct Biol* **116**, 71-76 (1996).
14. Mastronarde, D.N. Dual-axis tomography: an approach with alignment methods that preserve resolution. *J Struct Biol* **120**, 343-352 (1997).